ELUCIDATION OF HYDROGEN OXIDATION KINETICS ON METAL/PROTON CONDUCTOR INTERFACE

A Thesis
Presented to
The Academic Faculty

by

Shi Feng

In Partial Fulfillment
of the Requirements for the Degree
Master of Science in the
School of Materials Science and Engineering

Georgia Institute of Technology
Aug 2013

ELUCIDATION OF HYDROGEN OXIDATION KINETICS ON METAL/PROTON CONDUCTOR INTERFACE

Approved by:

Professor Meilin Liu, Advisor
School of Materials Science and Engineering
Georgia Institute of Technology

Professor Hamid Garmestani
School of Materials Science and Engineering
Georgia Institute of Technology

Professor Preet Preet
School of Materials Science and Engineering
Georgia Institute of Technology

Date Approved: 22 April 2013

To Mum and Dad,

for their interminable love.

ACKNOWLEDGEMENTS

Many people extended their valuable assistance in completing the work and the preparation of this dissertation. First and foremost, my sincere gratitude goes to my advisor, Dr. Meilin Liu, who made my education and research in Georgia Tech possible. He has been so insightful and knowledgeable in the field. And he provides the training, facilities, and everything I need to carry out my work. He taught me how to 'think' in research through patient instructions and consultation. To Dr. Liu, I am deeply indebted.

I would also like to thank Dr. Matthew Lynch. When I began working in Liu group, he took me under his wings and helped me get familiar with modeling. He served as a perfect role model and provided a great foundation where I started from. I am also grateful to Dr. Mingfei Liu for teaching me about experiments. His expertise in solid oxide fuel cells and enthusiasm in research constantly inspires me to proceed. My dear colleagues contributed in many ways. They ensure Liu group a thought-provoking place to learn and create. Thank Wenping Sun, Xiaxi Li and Liyi Li for collaboration. Thank Xian Qin, for encouragement and friendship.

Special thanks to Dr. Hamid Garmestani and Dr. Preet Singh for willingness to serve on my committee and for their very helpful suggestions.

Financial support from Samsung Advanced Institute of Technology and Heterogeneous Functional Materials (HetroFoaM) Center, Department of Energy, is greatly acknowledged.

To my parents, Ling Chen and Chaoli Feng. It is my mother who first introduced the beauty of science to me. Now as a junior member of academia, I strive to add a tiny contribution to human knowledge with deep reverence for nature.

TABLE OF CONTENTS

LIST OF TABLES

LIST OF FIGURES

LIST OF ABBREVATIONS

BCY $BaCe_{0.9}Y_{0.1}O_{3-\delta}$.

BZCY $BaZr_{0.1}Ce_{0.7}Y_{0.2}O_{3-\delta}$.

BZCYYb $BaZr_{0.1}Ce_{0.7}Y_{0.1}Yb_{0.1}O_{3-\delta}$.

BZY $BaZr_{0.9}Y_{0.1}O_{3-\delta}$.

DFT Density Function Theory.

EIS Electrochemical Impedance Spectroscopy.

EMF The Electromotive Force.

GDC $Ce_{1-x}Gd_xO_{2-x/2}$.

GNP Glycine Nitrate Process.

IT-SOFC Intermediate Temperature SOFC.

LSC $La_{1-x}Sr_xCoO_{3-\delta}$.

LSCF $La_{1-x}Sr_xCo_{1-y}Fe_yO_{3-\delta}$.

LSF $La_{1-x}Sr_xFeO_{3-\delta}$.

LSM $La_{1-x}Sr_xMnO_{3\pm\delta}$.

MCFC Molten Carbonate Fuel Cell.

MIEC Mixed Ionic Electronic Conductor.

OCV Open Circuit Voltage.

PAFC Phosphoric Acid Fuel Cell.

PCET Proton-electron Coupled Transfer.

PEM Polymer Electrolyte Membrane.

PLD Pulse Laser Deposition.

PSA Pressure Swing Adsoprtion.

RLS Rate Limiting Step.

SDC $Ce_{1-x}Sm_xO_{2-x/2}$.

SOFC Solid Oxide Fuel Cells.

SSR Solid State Reactions.

TPB Triple Phase Boundaries.

WGS Water Gas Shift.

YSZ Yttrium Stabilized Zirconia.

SUMMARY

High temperature proton conducting perovskite oxides are very attractive materials for applications in electrochemical devices, such as solid oxide fuel cells (SOFCs) and hydrogen permeation membranes. A better understanding of the hydrogen oxidation mechanism over the metal/proton conductor interface, is critical for rational design to further enhance the performances of the applications.

However, kinetic studies focused on the metal/proton system are limited, compared with the intensively studied metal/oxygen ion conductor system, e.g., Ni/YSZ (yttrium stabilized zirconia, $Zr_{1-x}Y_xO_{2-\delta}$). This work presents an elementary kinetic model developed to assess reaction pathway of hydrogen oxidation/reduction on metal/proton conductor interface. Individual rate expressions and overall hydrogen partial pressure dependencies of current density and polarization resistance were derived in different rate limiting cases.

The model is testified by tailored experiments on $Pt/BaZr_{0.1}Ce_{0.7}Y_{0.1}Yb_{0.1}O_{3-\delta}$ (BZCYYb) interface using pattern electrodes. Comparison of electrochemical testing and the theoretical predictions indicates the dissociation of hydrogen is the rate-limiting step (RLS), instead of charge transfer, displaying behavior different from metal/oxygen ion conductor interfaces.

The kinetic model presented in this thesis is validated by high quantitative agreement with experiments under various conditions. The discovery not only contributes to the fundamental understanding of the hydrogen oxidation kinetics over metal/proton conductors, but provides insights for rational design of hydrogen oxidation catalysts in a variety of electrochemical systems.

CHAPTER I

INTRODUCTION

In this century, the energy challenge continues to evolve with ever increasing world energy consumption. The complex situation of natural resource sustainability, climate change, population growth urges multi-discipline research to improve current technologies and offer new energy solutions.

Nowadays, fossil fuel still dominates the energy mix, with market share higher than 80% . Coal, natural gas and oil also constitute the primary source for electricity production, taking up more than 65% of total according to data of 2009 [6]. For the past decade, coal contributes to half of the increased energy expenditure and keeps growing [7]. In a 30 year projection, the consumption of petroleum and natural gas shall continue to grow in US. The domestic supply of fossil fuels is secured by the strong growth of shale gas/oil exploitation and unlock of light tight oil [8].

However, pollution and efficiency are the two major drawbacks of the traditional fossil fuel consumption in power plants and combustion engines. Alternatively, syngas produced by steam reforming of natural gas and the gasification of coal is a cleaner energy, which consists of hydrogen, carbon monoxide and some carbon oxide. Hydrogen is the next stage product from separation of syngas. While production from other resources is trivial, deriving hydrogen from fossil fuels facilitates a smooth transition to clean hydrogen energy. Both syngas and hydrogen can be used as feedstock for fuel cells to achieve high efficiency.

1.1 Fuel Cell Technologies

A major goal of energy engineers and scientists is to improve the utilization efficiency. Fuel cells are such devices that directly convert chemical energy in fuels to

electricity bypassing the conversion to heat and mechanical energy, thus achieving theoretical efficiency significantly higher than conventional engines.

All fuel cells share common components of anode and cathode separated by electrolyte. Fuel is fed to anode, losing electrons to circuit. Electrons travel through the external circuit, power the load and arrive at cathode to reduce the oxidant (O_2). Ion transport through the electrolyte balances the electron flow and completes the circuit, as shown in Figure 1. Half electrochemical reactions at two electrode interfaces are mediated by the ion conduction in the electrolyte, too.

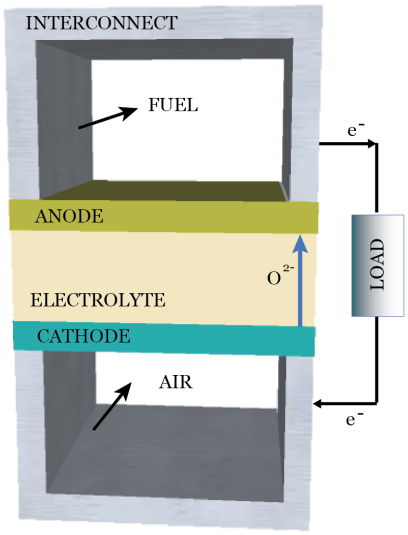

Figure 1: A unit cell in planar solid oxide fuel cell (SOFC) stacks

Electrolyte characterizes different fuel cells and mostly determines their operation temperature. Aqueous electrolyte fuel cells include alkali fuel cells (AFC) and phosphoric acid fuel cells (PAFC). In recent years more attention is paid to polymer electrolyte membrane (PEM, also known as proton exchange membrane) fuel cells, molten carbonate fuel cells (MCFCs) and SOFCs.

The operation temperature of fuel cells ranges from slightly above room temperature to as high as 1000 °C. PEM operates at 80-140 °C and PAFC at around 200 °C. MCFC and SOFC need higher temperature to activate conductivity, operating

at 500-700 °C and 600-1000 °C respectively. A comparison of fuel cell technologies is shown in Figure 2.

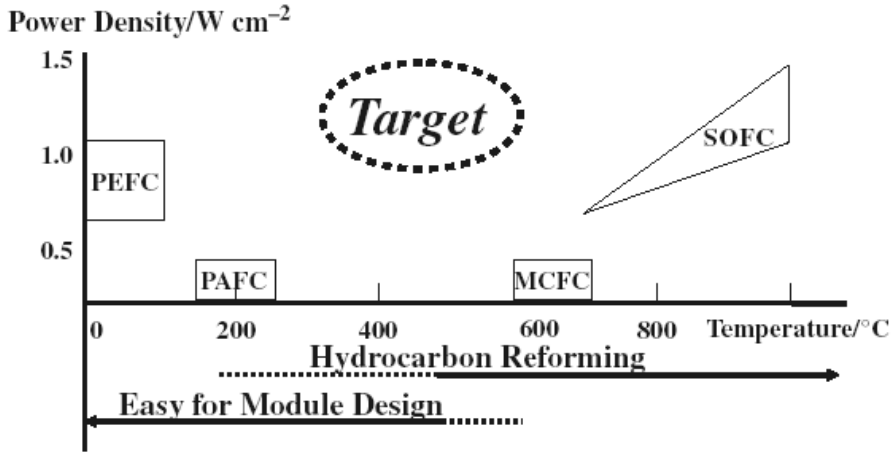

Figure 2: The target and status of fuel cell technologies [1]

PEM employs a thin layer of polymer proton conducting membrane as electrolyte. The morphology of the polymer network facilitates continuous transport of proton from anode to cathode when fully hydrated. The membrane is impermeable to gases and does not allow electron transport. The commercially available Nafion, a DuPont product, is the polymer of choice. Working temperature above 100 °C is desirable but may cause dehydration problem as water vapor pressure increases rapidly above 80 °C. To resolve the hydration issue Nafion can be modified by impregnating silica into the pores via in-situ reactions to form composite membranes [9].

AFCs are the best performing cells below 200 °C [10]. It employs alkaline solution as electrolyte. Hydrogen reacts with OH^-, generating water and electrons. Hydroxyl is replenished by the other half reaction between oxygen and water. AFCs have the advantages of high power densities, facile kinetics and non-reliance on noble metal catalysts. However, trace amount of CO_2 from the air stream will degrade the cell by reacting with the OH^- to form non-conducting carbonate precipitation. Current solution of improve CO_2 tolerance is to replace the KOH(aq) with solid alkaline

electrolyte membrane (AEM) to exclude metal cations [11].

Advantages of high temperature fuel cells, MCFCs and SOFCs, are enhanced efficiency and internal reforming of fuel gases with the heat from the operation of the fuel cells themselves. The system configuration is simplified without external reformers and efficiency is increased. The reforming processes is endothermic in total, consisting of two reversible reactions:

$$CH_4 + H_2O \rightleftharpoons CO + 3H_2 \text{ Methane Reforming}$$

$$CO + H_2O \rightleftharpoons H_2 + CO_2 \text{ Water Gas Shift (WGS)}$$

State-of-art electrolyte for MCFCs is eutectic $Li_2CO_3 - K_2CO_3$ mixture hold in place by porous $LiAlO_2$ matrix. Fuel gases reacts with CO_3^{2-} at anode side generating CO_2, H_2O and electrons. The anode exhaust gas is then burned, mixed with excess air and fed to the cathode, where oxygen and CO_2 accept electrons and form CO_3^{2-}. At 650 °C, non-precious metals such as nickel is sufficient to be catalyst.

SOFCs are characterized by the solid state ceramic electrolyte. Ceramics are corrosion resistant and cost-effective. The high operation temperature promotes reaction kinetics and at the other hand imposes more requirements for the materials and maintenance of the device. Anode and cathode have porous structure to allow gas flow to the reaction sites. Electrolyte is dense to prevent cross leakage of gases. Desirable electrodes have high electronic conductivity for current collection, while electrolyte has high ionic, either oxygen ion or proton conductivity. Another advantage is modularity. Unit cells are packed into stack to intensify power output. For application in vehicles, SOFC is the only fuel cell that can directly utilize liquid fuel without fuel processors. The goal of SOFC study is to lower operation temperature to intermediate range 600-800 °C compared to 800-1000 °C.

1.2 SOFC and Challenges

Since the first experiment in 1937 by Swiss scientist Emil Baur, SOFC has evolved for more than seventy years. Like other fuel cells, SOFCs are electrochemical devices that convert chemical energy into electricity and heat. SOFC configuration vary from tubular to planar, monolithic to segmented-cell-in-series [12], working on the same principles. Oxidation and reduction reactions occur at spatially separated terminals. Charged ionic species move through electrolyte which is deliberately designed to restrict electronic species from passing through. Using hydrogen as fuel, if the electrolyte is an oxygen ion conductor, water is produced at the anode side. Otherwise if it is proton conductor, water is produced at the cathode side where protons arrive to combine with oxygen ions.

Electrolyte for SOFCs are largely oxygen ion conductors, or oxygen vacancy conductors. Oxygen ion transport by hopping from one vacancy site to a neighboring one. The process is thermally activated. Electrolyte must operate at temperatures high enough to activate conductivity. The extensively used material is yttrium stabilized zirconia (YSZ). Pure ZrO_2 is not a good ion conductor itself. But after stabilization, Zr^{4+} being substituted by Y^{3+}, the concentration of oxygen vacancies increases significantly as the product of the doping defect reaction. Doping concentration between 8mol% to 10mol% is of interest because the highest ion conductivity falls into this range, and it meets the threshold requirement for the fluorite structure to be fully stabilized [12].

For intermediate temperature SOFCs (IT-SOFCs), the conductivity of YSZ is not sufficient. Doped ceria including $Ce_{1-x}Sm_xO_{2-x/2}$ (SDC) and $Ce_{1-x}Gd_xO_{2-x/2}$ (GDC) were developed to be alternative electrolyte material for their higher conductivities around 800 °C, one order of magnitude higher than YSZ. Pure CeO_2 exhibits n-type conductivity. When dopants introduce high oxygen vacancy concentration, the ionic conductivity becomes dominant [13]. However, at lower P_{O_2} near the anode side,

electronic conductivity rises again, which causes voltage loss [14].

The earliest cathode of SOFC was platinum exclusively. Then interest transferred to conductive transition metal oxides out of economic considerations [15]. Perovskite oxides, firstly $La_{1-x}Sr_xCoO_{3-\delta}$ (LSC) then $La_{1-x}Sr_xMnO_{3\pm\delta}$ (LSM) have been intensively researched since the 1960s and 1970s respectively. Since LSC is not chemically stable in contact with YSZ, LSM is the material widely used in the first-generation SOFC stacks. However, when temperature decreases from 1000 °C to intermediate range, the performance of LSM degrades rapidly. Then came the concept of triple phase boundaries (TPB) in attempt to replace LSM. LSM is electronically conductive but has limited ionic conductivity. The reduction of oxygen only takes place within a very narrow area near the boundary where the electronic phase, the ionic phase and gaseous phase all meet.

Perovskite mixed ionic electronic conductor (MIECs) perovskites in a single phase was proposed as the solution to expand the active reaction zone beyond TPB. The perovskite oxides generally have a ABO_3 structure. Engineering of the B-site dopants leads to recognition of MIECs such as $La_{1-x}Sr_xFeO_{3-\delta}$ (LSF) and $La_{1-x}Sr_xCo_{1-y}Fe_yO_{3-\delta}$ (LSCF). A larger portion of the surface becomes activated in the case of MIEC. They represent the current trend of cathode material research at target temperature below 800 °C.

As for stability, LSM is chemically compatible with YSZ. LSF, LSCF and LSC will react with YSZ and form insulating $SrZrO_3$ and(or) $La_2Zr_2O_7$. SDC and GDC are used as interlayer between YSZ and LSCF or LSC to prevent the reactions. Chromium poisoning is another issue for SOFC cathodes as Cr vapor is released from the metal interconnects of the stacks. Matsuzaki and Yasuda studied Cr poisoning of several cathode/electrolyte pairs. Performance of LSM/YSZ degrades immediately due to Cr^{3+} substitution. LSF, LSCF and LSC with YSZ will form $SrCrO_4$ in presence of Cr vapor, which leads to degradation as time evolves; whereas LSCF/SDC shows no

apparent degradation for 40 h [16].

The state-of-art anode materials for high temperature SOFCs are Ni-YSZ cermets. As a combination of metal and ceramic phases, the cermets display excellent conductivity and catalytic activity. The primary disadvantage of Ni-YSZ is the sulfur poisoning and carbon coking when fed with hydrocarbon fuels.

However, in intermediate temperature range, YSZ is not an adequate ionic conductor. Proton conductors are drawing more and more attention for the higher conductivity at temperature less than 750 °C. Among them $BaCeO_3$ and $BaZrO_3$ are of most interest as $BaCeO_3$ has high conductivity, and $BaZrO_3$ is more chemically stable in atmosphere containing CO_2. Toyota group has reported high power density ($0.9 \sim 1.4$ Wcm^{-2}) of proton conductor SOFC using $BaCeO_3$-based material running at 400 - 600 °C [17]. Proton conductors are not only promising electrolyte for fuel cells but also for hydrogen permeation membrane, too.

1.3 Hydrogen Permeation Membranes for Hydrogen Energy

Nowadays, the primary hydrogen source is the commercialized steam reforming process from fossil hydrocarbons. The reform technology is mature. But the concern is the hydrogen separation from the gas mixture. In an integrated hydrogen plant, the hydrogen separation unit has upstream coal gasifier, WGS reactor and downstream SOFCs or MCFCs output. Traditional separation applications include the recovery of hydrogen from the ammonia plant purge stream.

Currently widely used hydrogen purification techniques are pressure swing adsorption (PSA), cryogenic distillation and membrane separation. PSA is the state-of-art process, but has the disadvantage of being intensively energy consuming just like cryogenic distillation. PSA works at high pressure thus requires additional compression procedures. Membranes are promising alternatives which operate continuously at a much lower, potentially less than half cost of energy than PSA [18]. They are

also more spatially flexible, offering purification at different scales.

Membranes are selective barriers that allow the passage of certain components of a mixture and obstruct the others. There are four categories of hydrogen separation membranes: (i). polymeric, (ii). metallic, (iii). carbon and (iv). ceramic [19]. At present, only polymer membranes are considerably industrialized. The latter three inorganic materials are of engineering interest and under development.

Polymer membranes operate at temperatures below 110 °C. Gases are selected by different permeabilities (product of diffusivity and solubility coefficient), called solution-diffusion mechanism. The gases from the feed flow dissolve in the polymer, diffuse to other side, and desorb to the permeate flow. For a binary mixture of A and B, the selectivity is defined as

$$\alpha_{A/B} = \frac{P_A}{P_B} \tag{1.1}$$

where P_A and P_B are the permeabilities. Although they are the only membranes significantly commercialized. polymer membranes have drawbacks such as low selectivity; low flux; SO_x, CO_2, HCl poisoning; and mechanical deformation sensitivity thus reduced lifetime.

Metallic membranes have ultra high selectivity. Pd and Pd alloys exclusively allow hydrogen permeation, producing hydrogen of impurity less than 1 part per billion [20]. The separation is based on solution-diffusion mechanism, too. Hydrogen diffuses in the metal in the form of atoms and they recombine to molecules in the end. Commercial metallic membranes work at temperatures 300-600 °C and produce high purity H_2. In thermal cycling, an irreversible change of the Pd lattice takes place as a result of repeated transition between α and β phases. The change of the lattice structure damages the membrane. The application is limited by the high cost of palladium as well, which is twice as expensive as gold. The challenge of Pd/Pd alloy research is to minimize the Pd usage in the membrane and increase the sustainability.

Carbon membranes are porous membranes based on mechanism of molecule sieving or surface diffusion. Surface diffusion, as the name indicates, refers to the process that molecule migrate along the surfaces of the pores. It may happen with Knudsen diffusion in parallel and increase the selectivity by differentiating the adsorbing abilities. Molecule sieving happens when the pore size is so small that larger molecules are sieved out. The carbon membranes by molecule sieving is promising but has the drawback of brittleness. The performance degrades when strongly adsorping vapors such as H_2S, NH_3 or chlorofluorocarbons are present [21]. The performance also degrades with decreasing temperature as the pore sizes shrink. So far, carbon membranes are not economically feasible or sufficiently commercially available.

The focus of research is the ceramic membranes. They can be divided in two groups, (i). microporous ceramics and (ii). dense ceramics. Micropore is defined as pore size not exceeding 2.0 nm (IUPAC). Microporous ceramics include amorphous silica, its deriatives and non-silica material like zeolites. Silica-based materials select by combination of Knudsen diffusion and molecule sieving. Zeolites are reported to be shape-selective and surface-diffusion-selective [18].

Dense ceramic membranes has selectivity orders of magnitude higher than microporous ones. The working principle is solution-diffusion mechanism, too. Hydrogen molecule dissociates into atoms upon adsorption on the membrane. Protons migrates through the membrane and recombine into molecules at the permeate stream side, as shown in Figure 3. Theoretically, the selectivity is comparable to Pd/Pd alloy membranes since only hydrogen is permeable. But the cost of ceramics is much lower than Pd based membranes. The ceramic membranes also have the advantage of durability and stability in steam, CO, CO_2, and H_2S [3]. Operating at high temperatures, the membrane has fast kinetics and is able to produce industrially significant flux. One approach of development is the mixed conducting acceptor-doped cerates and zirconates [22]. Another approach is mixing ceramic ($BaCeO_3$, Al_2O_3, ZrO_2,

etc) with metal to form composite cermets. At 900 °C, ceramic-metal cermets have demonstrated hydrogen flux as high as 20 $cm^3/min \cdot cm^2$ nongalvanically in ambient hydrogen pressure. The cermet membrane ran for 190 h and showed no noticeable degradation in syngas atmosphere [23]. In industrial practice, flux rate is hopefully to be increased to $> 200 cm^3/min \cdot cm^2$ under high pressure. With all the advantages, dense ceramic membranes are promising for long term hydrogen separation in real-world coal gas conditions.

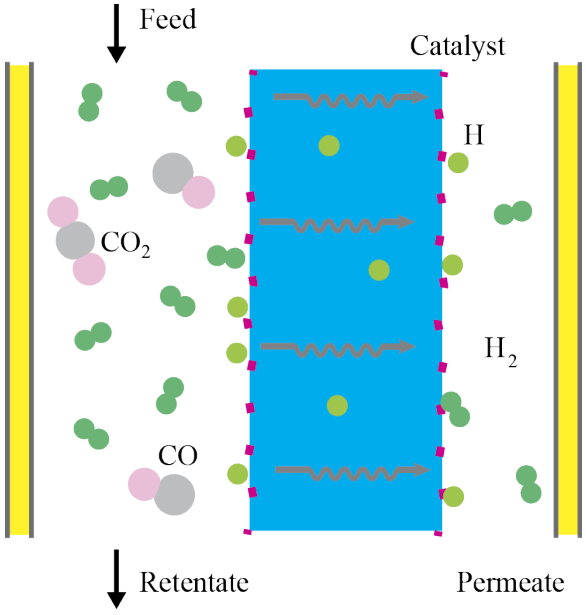

Figure 3: Dense ceramic membrane reactor for hydrogen separation from syngas

1.4 Motivation

High temperature proton conducting perovskite oxides are very attractive materials for applications in electrochemical devices, such as hydrogen sensors, fuel cells, hydrogen separation, electrolysis, electrochemical reactors, etc [3, 24–26]. Among the perovskite oxides investigated, yttrium and ytterbium co-doped barium cerate and zirconate, $BaZr_{0.1}Ce_{0.7}Y_{0.1}Yb_{0.1}O_{3-\delta}$(BZCYYb), has recently received growing attention [3, 27, 28].

BZCYYb not only shows the highest ionic conductivity in intermediate temperature range (500 750 °C), but also exhibits excellent chemical stability under CO_2 , H_2O and even H_2S [3]. It was reported to be stable in H_2 atmosphere containing 50vol%CO_2 or 50vol% H_2O at 750 °C. When mixed with a metal phase, such as Ni, to form composite cermet, it is an ideal anode for intermediate temperature SOFCs (porous) or membrane for hydrogen separation (dense). In both case, the hydrogen will be adsorbed, dissociate, and be oxidized on the porous or dense cermet surface. A better understanding of the hydrogen oxidation mechanism over the metal/BZCYYb interface, is necessary for rational design of the cermet to further enhance the performances of the fuel cell system or hydrogen separation membrane.

Compared with the metal/BZCYYb system, the hydrogen oxidation mechanism over oxygen ion conductor based Ni/YSZ has been intensively studied [29–33]. It is generally believed and experimentally supported that reactions take place at TPB [33,34]. As for the mechanism, the hydrogen spillover pathway is better accepted over oxygen spillover, hydrogen interstitial, hydroxyl spillover, etc., despite the controversy [30,35]. An interesting and counter-intuitive phenomenon is that the increase of P_{H_2O} in the gas composition promotes the reaction kinetics [30, 33, 34].

However, the studies focused on the metal/proton conductor system are limited. D. Kek et al. studied the effect of electrode material on the metal/$Sr_{0.995}Ce_{0.95}Y_{0.05}O_{2.97}$ interface. Kek found that the hydrogen oxidation reaction mechanism depends on the nature of the electrode material rather than the electrolyte surface [36–38]. The apparent reaction order suggests that Ni electrode is rate-limited by adsorption and diffusion of H_2, Au by dissociation or diffusion of H, while Ag and Pt lie in between. Zisekas et al. investigated the electrode kinetics at the porous Pd/proton conductor interface, using $SrCe_{0.95}Yb_{0.05}O_{3-a}$ and $SrZr_{0.95}Y_{0.05}O_{3-a}$. They concluded that the electrode kinetics depends on the proton-conducting phase and SCY exhibits much faster kinetics, with four times higher exchange current density [39]. Akoshima et

al. tested screen-printed porous Pt electrode on proton conductor $BaCe_{0.95}Y_{0.05}O_{3-\delta}$ (BCY). The electrode interfacial conductivity was discovered to be strongly determined by hydrogen partial pressure and insensitive to water vapor pressure P_{H_2O}. P_{H_2O} had little effect on the conductivity of electrolyte, too. They proposed two reaction models and suggested the rate limiting processes are 1). diffusion of H_{atm} near TPB and 2). dissociative adsorption of hydrogen in parallel [40].

Despite the fragments of reports, a clear understanding of the reaction mechanism is still lacking. This work proposes an elementary reaction sequence of hydrogen oxidation/evolution adopting proton-electron coupled transfer (PCET) assumption [41]. The objective is to locate one rate limiting step of the sequence. To isolate mechanism and to eliminate the complexity of microstructure, a well-defined Pt pattern electrode on BZCYYb instead of porous electrode is to be used. By the utilization of pattern electrodes experiments can precisely control the exposed area of ceramic and the length of TPB. The predictions of the model validated by electrochemical testing shall add to the current knowledge of hydrogen oxidation mechanism on metal/proton conductor interface.

CHAPTER II

FABRICATION AND OPTIMIZATION OF BZCYYB

2.1 BZCYYb – the Proton Conductor

2.1.1 Proton Conductor vs. Oxygen Conductor

Proton conductors are more promising electrolyte candidates for intermediate temperatures (600 - 800 °C) because of the smaller activation energy of proton conduction. Oxygen conductor such as YSZ and doped cerate (SDC, GDC, etc.) have high conductivity at elevated temperatures (> 1000 °C). However, the exponential dependency on activation energy in Arrhenius equation causes the rapid decrease of oxygen conductivity.

$$\sigma = \sigma_0 exp\left(-\frac{E_a}{RT}\right) \tag{2.1}$$

Activation of typical ceramic oxygen conductor and proton conductor are listed in Table 1. Fabrication methods affect the activation energy as they create different grain sizes. Proton conduction needs water in the atmosphere to produce the protonic defect $OH_O^{\cdot}$. As seen from Table 1, the activation energy for proton conductor is of $0.3 \sim 0.5$ eV, much smaller than the $0.7 \sim 1.4$ eV of oxygen conductors. Therefore for intermediate temperature, proton conductors show higher conductivity.

2.1.2 The Perovskite Proton Conductors

Perovskite oxide is a large family of materials that display a variety of properties, such as semiconductivity, ferroelectrictity and superconductivity. Typical perovskite oxide has ABO_3 formula, with a larger 12-coordinated ion at the A-site, and a 6-coordinated ion at B-site. The valence combination includes $A^{+}B^{5+}O_3$, $A^{2+}B^{4+}O_3$ and $A^{3+}B^{3+}O_3$. Ideal perovskite has cubic lattice, which requires the radii of A, B and O ions to match. Otherwise, the lattice deviates from cubic to tetragonal or

Table 1: Activation energy of oxygen and proton conductors

Oxygen Conductor	Composition	Technique	E_a/eV	Ref.
YSZ	$Zr_{0.84}Y_{0.16}O_{2-\delta}$	Spray pyrolysis	0.9	[42]
		Spin coating	1.1	[43]
GDC	$Ce_{0.8}Gd_{0.2}O_{1.9-\delta}$	Spray pyrolysis	0.7	[44]
		Spin coating	1.3	[45]
SDC	$Ce_{0.8}Sm_{0.2}O_{1.9-\delta}$	Dry press	0.8	[46]
		Dry press	1.4	[46]
Proton Conductor	Composition	Atmosphere	E_a/eV	Ref.
BZG	$BaZr_{0.9}Gd_{0.1}O_{3-\delta}$	23hPa H_2O-N_2	0.5	[47]
BZS	$BaZr_{0.9}Sc_{0.1}O_{3-\delta}$	23hPa H_2O-N_2	0.5	[47]
BCY	$BaCe_{0.9}Y_{0.1}O_{3-\delta}$	23hPa H_2O-N_2	0.5	[48]
BZY	$BaZr_{0.9}Y_{0.1}O_{3-\delta}$	23hPa H_2O-N_2	0.4	[49]
BZCY	$BaZr_{0.1}Ce_{0.7}Y_{0.2}O_{3-\delta}$	wet $4\%H_2 - Ar$	0.4	[50]
BZCYYb	$BaZr_{0.1}Ce_{0.7}Y_{0.1}Yb_{0.1}O_{3-\delta}$	$3\%H_2O$-H_2	0.3	[51]

orthorhombic. A tolerance factor t is defined to describe the deviation

$$t \equiv \frac{r_A + r_O}{\sqrt{2}(r_B + r_O)} \tag{2.2}$$

For cubic structure $t = 1$.

Because of the diversity and the high temperatures stability, perovskites find applications in almost every component of SOFC: cathode (LSM, LSCF), electrolyte (BZY, BCY), anode ($SrTiO_3$) and interconnector ($LaCaCrO_3$). The oxygen and electronic conductivity of perovskites had been known. It was not until 1980s that first significant study on perovskite proton conductors ($LaYO_3$, $SrZrO_3$) were initialed by Iwahara [52]. Among the early discovered proton conductors, $SrCeO_3$ and $BaCeO_3$ demonstrated higher conductivities [52,53]. Despite the fact that both cerates tend to decompose into binary oxides and tend to react with even low amount of CO_2 [54,55], $BaCeO_3$-based materials were preferred and systematically researched.

The origin of proton conduction is the formation of protonic defects from the

dissociation adsorption of water

$$H_2O + V_{\ddot{O}} + O_O^x \rightleftharpoons 2OH_O^{\cdot} \tag{2.3}$$

The difference of electronegativities of A and B cations was found to be correlated with the enthalpy of the hydration reaction. The smaller the difference is, the more exothermic the reaction is [2]. Since the A-site cations Sr and Ba have similar electronegativities, the B-site cations have larger variation and effect. Study shows that as the B-site cations move in the direction of increasing electronegativities, Zr $\rightarrow$ Nb $\rightarrow$ Sn $\rightarrow$ Ti, the reaction constant decreases [56].

In the solid, proton is attached to a lattice O_O^x to form $OH_O^{\cdot}$ and forming hydrogen bond OH $\cdots$ O with an adjacent lattice O_O^x. Proton migrates in the lattice by hopping from one O_O^x to another. Meanwhile, the attachment of proton causes the nearest neighbor OH-O and OH-B separation to deviate. The hydrogen bond with a particular neighboring O_O^x breaks and reforms with another neighboring one dynamically [48]. Figure 4 shows the traces of proton around O sites and the interaction with O_O^x neighbors. The stability of the protonic defects is associated the reaction enthalpy

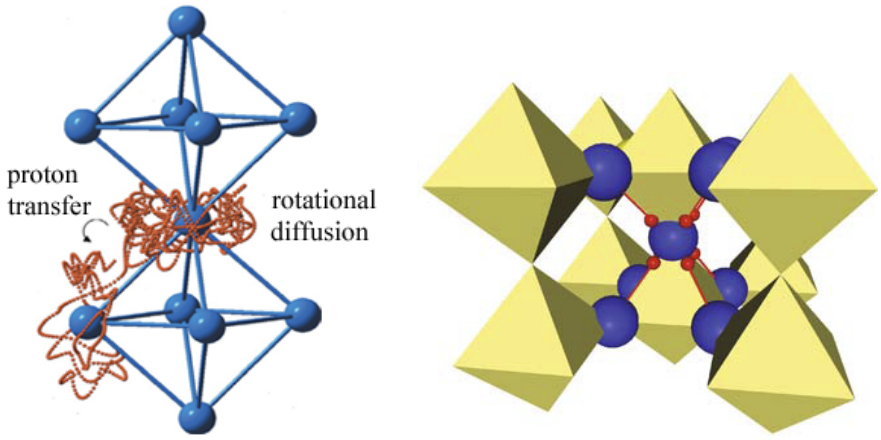

(a) (b)

Figure 4: Proton conduction in the perovskite lattce. a). the proton transfer mechanism [2], b). the interaction of OH $\cdots$ O [1]

of Rxn. 2.3. The stability of the oxides is associated with its tolerance against

CO_2, as they tend to decompose into carbonate in contact with CO_2. The stability against CO_2, $SrTi_{0.98}Sc_{0.02} > BaZrO_3 > BaCeO_3$, opposites the trend of proton defects stability [56].

As a compromise of $BaZrO_3$'s chemical stability and $BaCeO_3$'s high conductivity, solid solution of $BaZrO_3 - BaCeO_3$ was studied. According to Eq. 2.3, more oxygen vacancy is beneficial for creating protonic species. The strategy is to dope three valence cation doping in B(IV)-sites. Take Y for example, the defect equation writes

$$Y_2O_3 + 2AO \rightleftharpoons 2A_A^x + 2Y_B' + V_O^{\cdot\cdot} + 5O_O^x \tag{2.4}$$

The $BaZrO_3 - BaCeO_3$ solution based material BZCY shows improved chemical stability against CO_2 with Zr content [57] and high conductivity when Zr/Ce ratio is low [58].

In B-site dopants engineering, many trivalent rare earth metals were tested and compared, including Yb, Y, Gd, Nd, and La [59]. As the ion radius increases, on one hand the increased free volume allows more room for ionic transfer, on the other hand the distorted lattice hinders the ion mobility [60]. The optimized dopant is a trade-off of free volume and lattice symmetry [59].

Su et al. discovered that the addition of a second dopant to B-site increases the ionic conductivity of barium cerate to higher than each of the single-doped ones [61]. Recently in 2009, Yang et al. invented the Y and Yb co-doped BZCYYb which further enhanced the conductivity of barium cerate compared to BZCY. In temperature lower than 750 °C, BZCCYb has conductivity higher than benchmark oxygen conductors YSZ and GDC in wet oxygen (3vol% H_2O), as shown in Figure 5. In addition, when BZCYYb is used in Ni-BZCYYb cermet anode, the performance shows no degradation in the time span of 50 h against carbon coking and sulfur poisoning [3]. The desirable carbon coking tolerance was attributed to the BaO nano-islands formed on the Ni surface, which adsorbs water and promotes the water-mediated carbon removal [62].

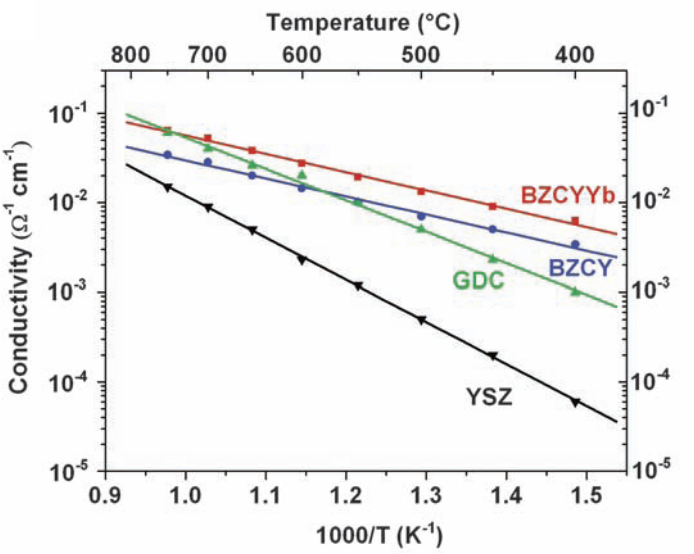

Figure 5: Ionic conductivity of BZCYYb, BZCY, YSZ and GDC [3]

2.2 Fabrication of BZCYYb

There are two methods for fabrication of BZCYYb: (i). solid state reaction (SSR) and (ii). glycine nitrate process (GNP). SSR produces BZCYYb with better stoichiometry, while GNP is faster and produces powder with smaller particle sizes.

Solid state reactions is commonly used powder synthesis method. Precursor solids are well mixed and react at elevated temperatures. For BZCYYb, the precursors are $BaCO_3$, ZrO_2, CeO_2, Y_2O_3 and Yb_2O_3, as listed in Table. 2.

Table 2: The precursors for BZCYYb SSR synthesis process

Solids	Item	Stoichiometric Ratio	Weight Ratio
$BaCO_3$	Sigma Aldrich #237108, $\geq$ 99%	1.0	197.34
ZrO_2	Alfa Aesar #44886, $\geq$ 99%99%	0.1	12.32
CeO_2	Sigma Aldrich #211575, $\geq$ 99.9%	0.7	120.48
Y_2O_3	Alfa Aesar #11181, $\geq$ 99.99%	0.05	11.29
Yb_2O_3	Alfa Aesar #11191, $\geq$ 99.9%	0.05	19.70

The solids were mixed, ball-milled in ethanol for overnight, dried in oven at 60 °C for 24 h, milled and calcined at 1100 °C for 10 h. To obtain purer phase, the calcination was repeated. To reduce the evaporation of BiO, the crucible was covered

with lid.

2.3 Densification of BZCYYb with Nickel Doping

To obtain a dense ($> 96\%$ relative density) electrolyte phase, originally BZCYYb pellets were sintered at very high temperature 1550 °C for 10h [3]. In literature, various agents were tested to aid the sintering of barium zirconate and barium cerate, such as ZnO, NiO, and Al_2O_3. Liu et al. reported that with 1wt% NiO doping, BZCYYb sintered at 1350 °C for 3h achieves 96% theoretical density. Doped BZCYYb pellets sintered 1450 °C for 3h shows similar open voltage as the non-doped ones sintered at 1550 °C for 10 h [63].

As pattern electrode substrate, BZCYYb electrolyte is desired to be as dense as possible. Following the routine of Liu, we tested sintering condition of BZCYYb with different nickel content. In the experimental groups, BZCYYb powders fabricated by SSR was mixed with $NiCO_3$, which decomposes to NiO at high temperature. Pellets were sintered at 1450 °C for 5 h, and polished to compare porosity. Three groups were tested:

(i). 1wt% NiO content, by mixing BZCYYb and $NiCO_3$ in weight ratio 99:1.589.

(ii). 0.5wt% NiO content, by mixing BZCYYb and $NiCO_3$ in weight ratio 99.5:0.795.

(iii). Undoped BZCYYb, the control group.

The $NiCO_3$/NiO dopant gives BZCYYb pellets black color, compared with pure BZCYYb's light brown. The NiO-BZCCYb becomes soft during one stage of the sintering process and tends to bend. To obtain flat NiO-BZCYYb pellets, they have to be placed on a flat substrate, e.g. a sintered blank BZCYYb pellet. NiO-BZCYYb pellets also tend to bond together when stacked. Pure BZCYYb powder must be scattered between pellets to prevent the clumping.

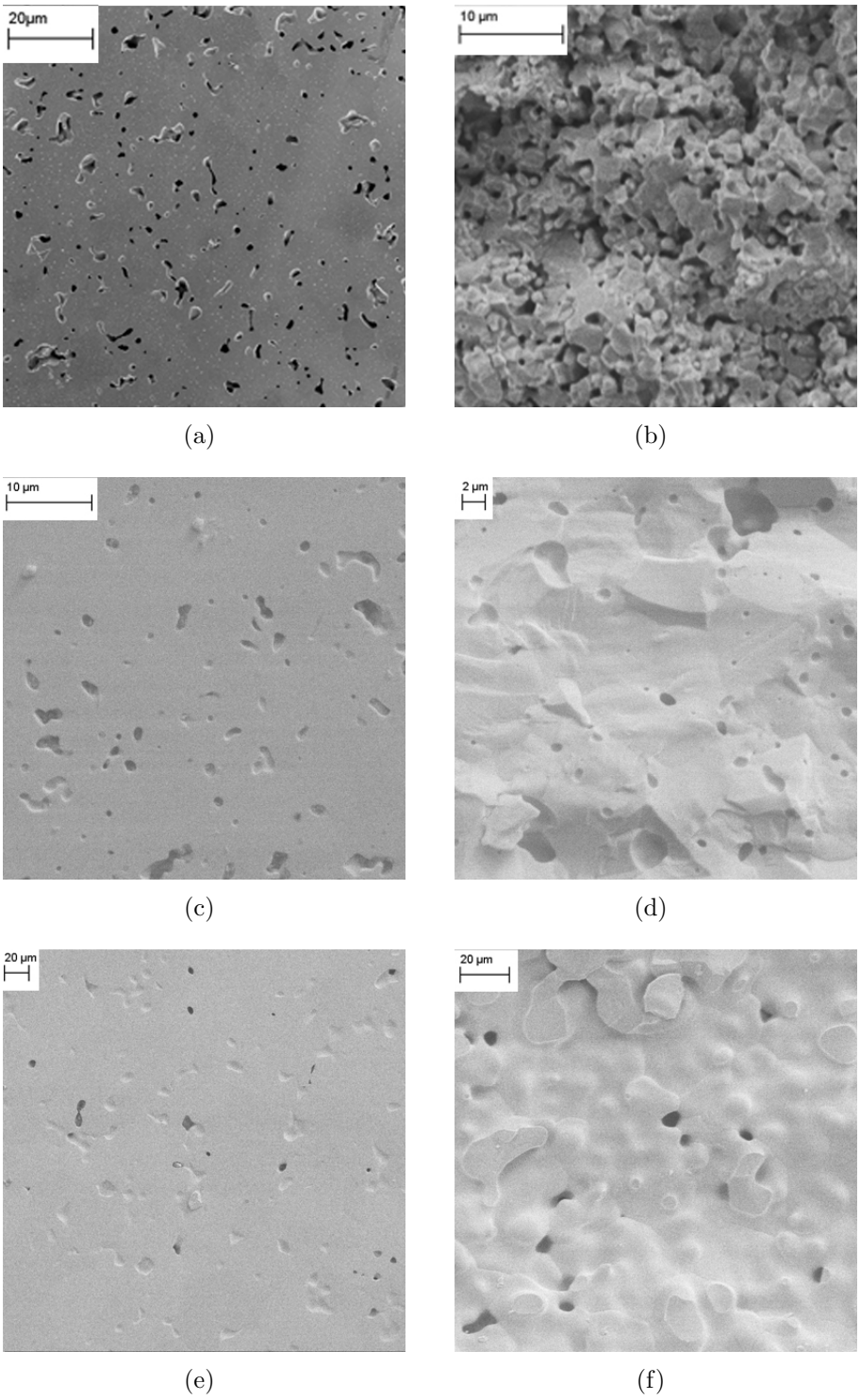

Figure 6: Porosities of BZCYYb with different NiO doping:
a). top surface and b). cross-section view of blank BZCYYb; c). top surface and d). cross-section view of 0.5wt% NiO-BZCYYb; e). top surface and f). cross-section view of 1wt% NiO-BZCYYb.

As seen from the top and cross-section view in Figure 6, the nickel content increased the density of BZCYYb pellets. The porosity decreased with increasing nickel. The 1wt% NiO-BZCYYb sintered at reduced temperature and time has satisfactory low porosity. No more nickel is to be added because it will distort the lattice.

XRD spectroscopy of blank BZCYYb and 1wt% NiO-BZCYYb powder is shown in Figure 7. The BZCYYb powder has single phase and displays characteristic perovskite peaks similar to that of $BaZr_xCe_{0.9-x}Y_{0.1}O_{3-\delta}$ (BZCY) powders [64].

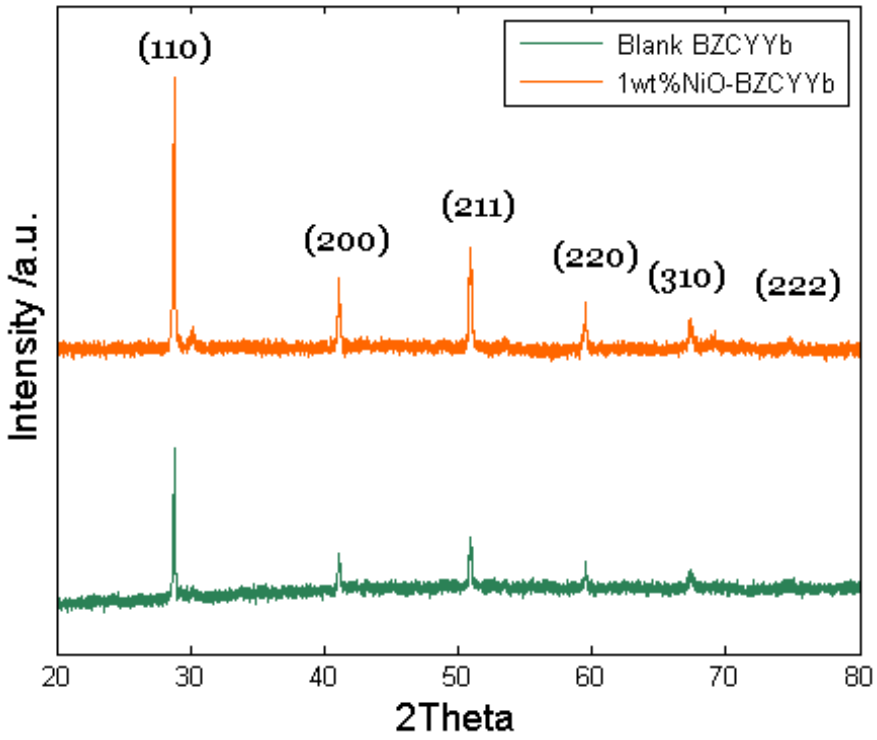

Figure 7: XRD pattern of BZCYYb and 1wt% NiO-BZCYYb powder

There is no $BaCeO_3$ peak in the diffraction patterns, which is present in the XRD of BZCYYb produced by citric acid-nitrate gel combustion process, as barium reacts with CO_2 from burning of the residual carbon in the grey powders. There is no NiO peak in the NiO-BZCYYb pattern, either, as the doping amount is small.

2.4 Summary

This chapter introduces the development of perovskite proton conductors, the invention of BZCYYb, and the fabrication method of high purity BZCYYb powder. Blank BZCYYb has to be sintered at high temperature (1550 °C) for long time (10 h). Testing of different NiO doping shows that 1%wt NiO content reduces the porosity of BZCYYb electrolyte at a lower sintering cost, 1450 °C for 5h.

CHAPTER III

FABRICATION OF PATTERN ELECTRODE

3.1 Impact of TPB

The concept of TPB is significant for electrode reactions, especially for the surface path. Take cathode for example, surface path describes the reaction sequence of: (i). oxygen adsorption onto the surface of cathode, (ii). adsorbate oxygen migrates along the surface to TPB, and (iii). the TPB incorporation reaction. In bulk path, oxygen incorporates into the lattice right after adsorption, skipping the surface transport. The two paths are illustrated in Figure. 8.

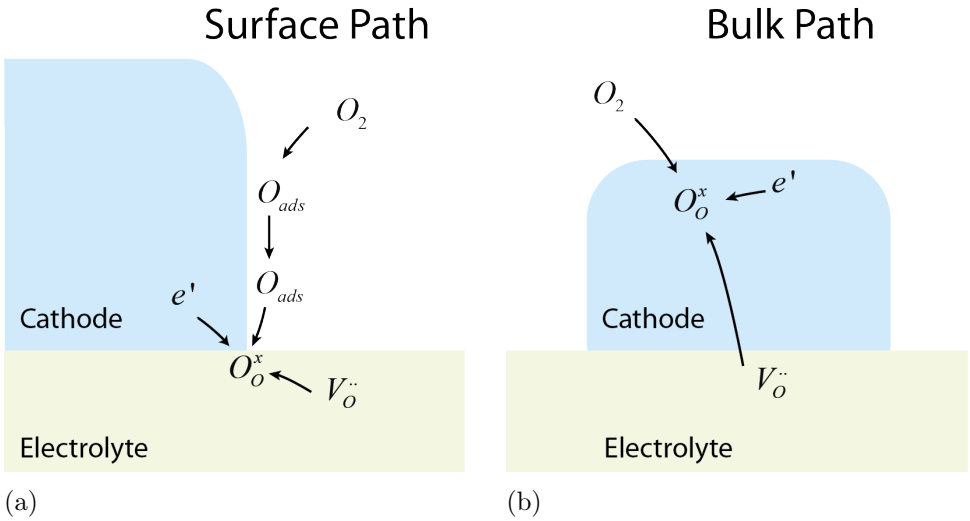

Figure 8: Comparison of surface path vs. bulk path

In the surface path, the incorporation reaction is confined to a narrow region close to the TPB, where electrons and oxygen vacancies are readily accessible. Similarly for anode reaction, the fuel species have access to oxygen ion and electronic conductive phase to lose electrons near TPB.

The performance of electrodes are not only determined by the intrinsic properties of the materials, but also by their microstructure. TPB density is one of the most significant factors of the microstructure. Single phase electrodes have limited electrode/electrode contact. One strategy to increase TPB density is to make porous composite electrodes on top of the dense electrolyte phase, as illustrated in Figure. 9

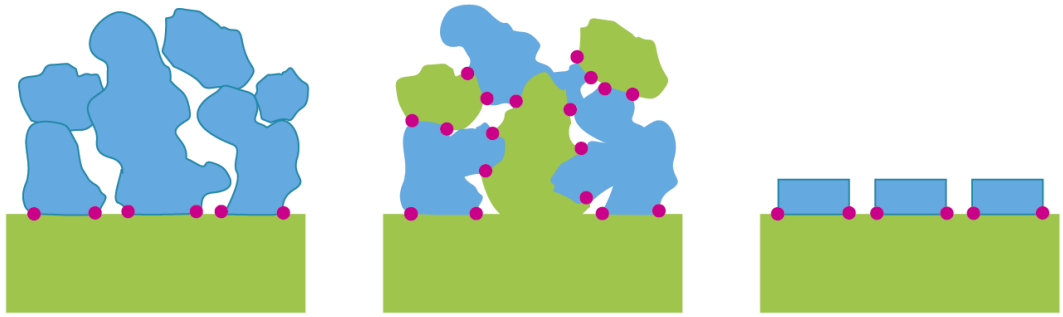

Figure 9: Electrode morphologies: (a). single phase electrode, (b). composite electrode, and (c). pattern electrode, TPB marked by dots.

That is where the concept of pattern electrode comes from. In reaction mechanism studies, the TPB length needs to controlled to exclude the interference of microstructure. Patterned electrode are also used in SOFC modeling as a simplification of the complex geometry [65–67]. The current should be correlated to TPB except in a few cases when bulk path is dominating, the electrode is thin and has good conductivity [66].

Experimental work by Mizusaki first normalized current density with TPB length [68]. TPB length was estimated according to averaged pore sizes measured from interface cross-section. This method does not offer sufficient precision to quantify the relation between performance and TPB length. Other studies used needle tip microelectrode probed into the electrolyte to create a rough ill-defined circular phase boundary [69]. Alternative microelectrode technique used pulse laser deposition (PLD) to sputter circular Pt electrodes of diameter $10 \sim 250\ \mu m$ [70, 71]. This method relies

on delicate mechanical contact of the electrode and current collector (a sharp tip), resulting in unstable contact resistance. Considering the usually large impedance ($\sim 10^7\ \Omega$), the variation caused by mechanical contact is substantial.

As the experimental effort to quantify TPB continued, Mizusaki et al. developed Ni pattern electrode on YSZ via photolithography. The interface conductivity was discovered to be linearly correlated to the TPB length [33, 72]. The proportionality was verified by Gauckler [73]. The capacity of pattern electrode, i.e. the TPB length density is largely associated with feature size. Koep improved the capacity by reducing the feature size to 2 μm from previously 20 μm [74].

3.2 Fabrication of Patttern Electrode

We use three methods to fabricate pattern electrode: the copper grid method, the embedded mesh method and photolithography.

3.2.1 Copper Grid Method

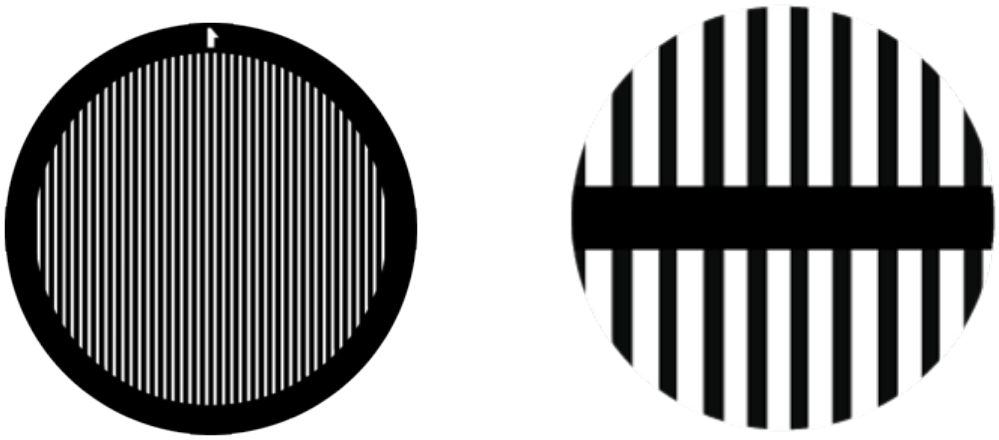

(a) (b)

Figure 10: Copper grid for pattern electrode

Copper grid mesh method uses DC magnetron sputtering to deposit metal such as Ni and Pt onto a ceramic substrate. Figure 10 shows the grid. The shape of grid is limited. Only discrete stripes can be fabricated. To create a connected criss-cross

network, a second layer of grid needs to be placed above or below. A metal bar in the middle is used to physically fix the grid, thus blocks the premier central part of the pattern, as shown in Figure 11.

In Figure 10, black part blocks the sputtering. Metal is sputtered through the white slots. Since the grid is held above the substrate to a distance, there is shadow effect resulting in unclear edge. Figure 11 shows the Ni pattern electrode of 200 nm thick. The pattern smears close to the edge, which makes it difficult to control TPB.

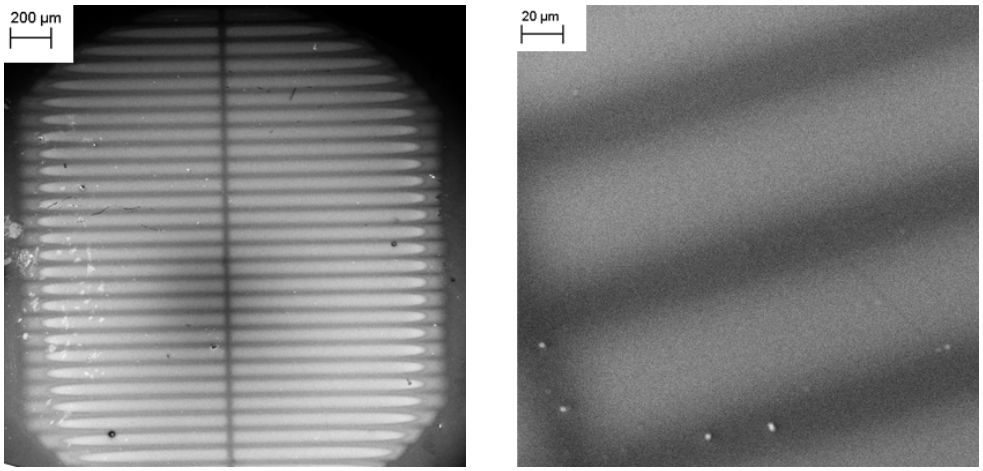

(a) (b)

Figure 11: SEM image of Ni pattern electrode

The TPB density from copper grid method is high, $\sim 2 \times 10^4$ m^{-1}. However, the commercially available grid has limited size, only 3 mm $\times$ 3 mm. On a pellet of diameter 1.1 cm, only 9% of surface was covered. Though copper grid method is time and cost effective, it is not suitable for SOFC reaction mechanism research.

3.2.2 Embedded Mesh Method

In embedded mesh method, metal mesh such as Pt and Ni, is embedded in powder and dry pressed into green pellet. The pellet is then sintered at high temperature in protection atmosphere, 4% H_2 balanced by Ar or N_2.

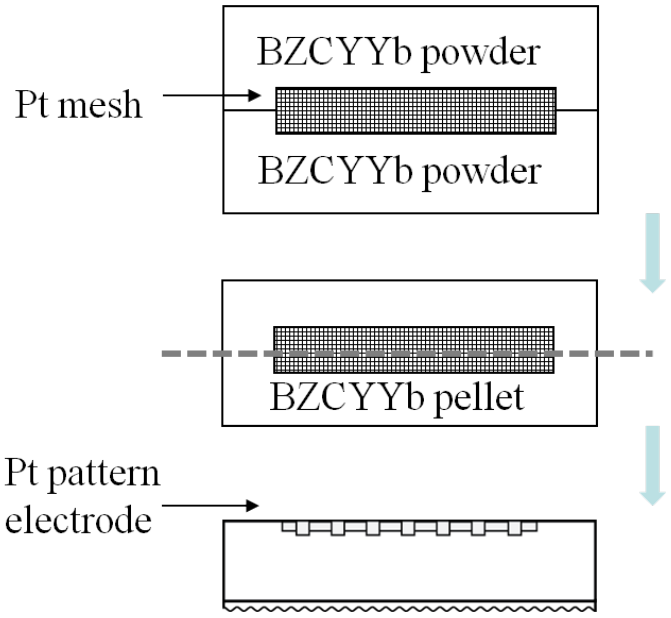

Figure 12: Pattern electrode fabrication by embedded mesh method

Figure 12 shows the procedure of embedded mesh method. The green pellet is about 2 mm thick with metal mesh in middle. Next, by polishing the top half off, the mesh is exposed on the surface. That is the pattern electrode. The pattern size is controlled by cutting of the mesh. The feature size is determined by the mesh itself. A 5 mm $\times$ 5 mm mesh has $\sim$ 20% coverage on a 1.1 cm diameter pellet. The TPB density is about 2×10^3 m^{-1}. The embedded mesh method has good reproducibility. It is useful for quickly producing $\sim$ 10 pellets in one batch. The disadvantage is that only selected metal has commercially available mesh, typically Pt and Ni. Ni has lower melting point (1453 °C), not able to sustain the high sintering temperature of BZCYYb. We used embedded Pt mesh to fabricate pattern electrode for verification of the model proposed in this thesis. The SEM image of Pt pattern is included in Section 5.2

3.2.3 Photolithography

Photolithography is widely used technique to fabricate pattern electrode with sharp edge and accurate feature size. for a pellet of diameter 1.1 cm, the size of the

inscribed square is 7.8 mm. Pattern size of 6 mm × 6 mm offers 30% coverage and allows some room for misalignment. Mask with 6 μm wide stripe and 3 μm gap in between produces TPB density of 1.8×10^5 m^{-1}, one order of magnitude higher than the copper grid method. For a 6 mm × 6 mm pattern, the overall TPB length is 8 m. With varying stripe/gap width, a variety of TPB density can be created. To reduce sheet resistance in current collection, the pattern is designed to be interconnected. Using positive photoresist, the pattern is a print of the dark part shown in Figure 13.(a).

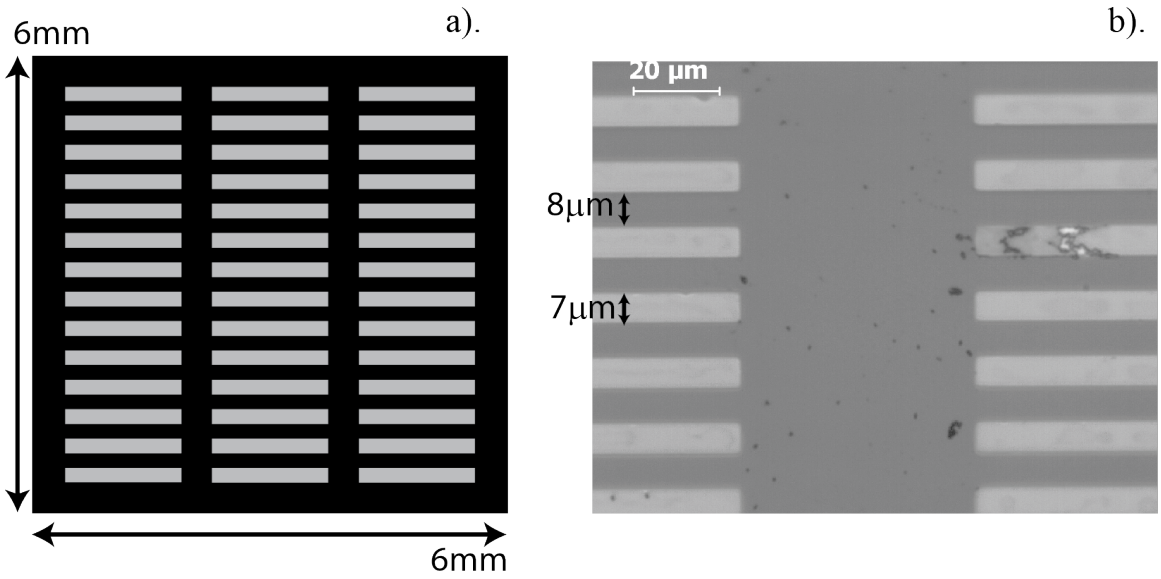

Figure 13: The mask for photolithography: a). schematic drawing and b). optic microscope with TPB density of 13.3m/cm^2

Figure 14 illustrates the fabrication procedure. First, positive photoresist P-20 (HMDS) was applied onto polished BZCYYb pellets by spin coating. The photoresist of 1.7 μm thickness was then prebaked at 115 °C and exposed to UV light (405 nm, 450 mJ/cm^2) through a set of masks of designated geometry and patterns, as shown in Figure 13. The exposed photoresist became soluble in MF-319 developer. After being soaked in the developer overnight, the photoresist exposed to UV light were dissolved. UV ozone was used to remove the residual on the exposed ceramic surface. Afterward, metal was deposited onto the sample through DC sputtering, covering the

entire sample surface. Immersing the samples in Resist Remover 1165 overnight lifted off the patterned photoresist along with the metal attached to it, while the metals on the areas with no photoresist remained. At last, the deposited metal reproduced the patterns of the transparent regions in the masks (the darker part in Figure13(a).

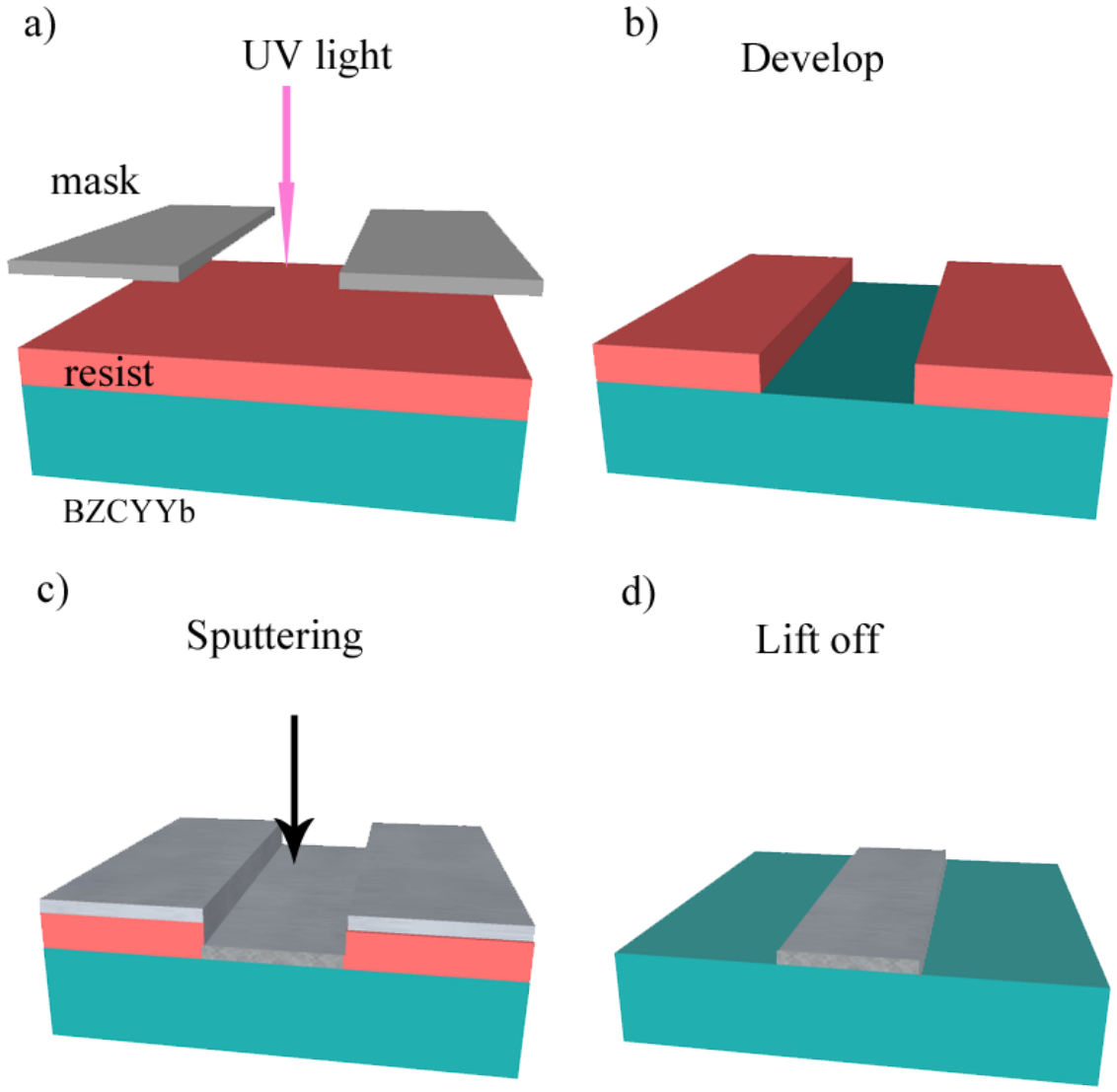

Figure 14: The procedure of pattern electrode fabrication by photolithography

The 1.7 μm thick resist gives sharp edge to the 200 nm thick electrode. Photolithography method has the best reproducibility and creates identical pattern each time. It also offers the capacity of fabricating different metal patterns in combination

of DC sputtering. The disadvantage is cost and time consuming. To compare the catalytic activity of different metals, photolithography method is the best choice.

3.3 Summary

TPB is very important characteristic parameter of the electrode microstructure, especially for the surface path of the electrode reactions. Pattern electrode was invented to achieve well-defined and measurable TPBs for quantitative correlation studies. Study on reaction mechanism needs pattern electrode to isolate the influence of microstructure. This chapter discusses three methods of pattern electrode fabrication. Copper grid method offers intermediate TPB density but suffers from edge shadow effect. Embedded mesh method is cost and time effective, has sharp edge contrast but the choice of metal is limited. Photolithography method produces the highest TPB density, has good edge contrast, but is the most time consuming. In practice, the latter two methods are more suitable for SOFC and hydrogen permeation membrane catalyst related studies.

CHAPTER IV

KINETIC MODEL OF HYDROGEN OXIDATION/REDUCTION ON METAL-BZCYYB INTERFACE

4.1 Thermodynamics

4.1.1 Concentration Cell

Assuming continuous oxygen and hydrogen supply at cathode and anode in SOFC operation condition, the separated half reactions are

$$\frac{1}{2}\mathrm{O_2} + 2\mathrm{e^-} = \mathrm{O^{2-}} \tag{4.1}$$

$$\mathrm{H_2} + \mathrm{O^{2-}} = \mathrm{H_2O} + 2\mathrm{e^-} \tag{4.2}$$

The overall reaction is

$$\mathrm{H_2} + \frac{1}{2}\mathrm{O_2} = \mathrm{H_2O} \tag{4.3}$$

The electromotive force (EMF) of the cell is given by the Nernst potential

$$E = \frac{RT}{4F} ln \frac{P_{O_{2,c}}}{P_{O_{2,a}}} \tag{4.4}$$

where R is the gas constant, F the Faraday's constant, the subscript c and a represent the cathode and anode.

At open circuit, the system is in equilibrium. The $P_{O_{2,a}}$ is calculated from equilibrium condition of anode.

$$P_{O_{2,a}} = \left(\frac{P_{H_2O}}{P_{H_2} K} \right)^2 \tag{4.5}$$

where K is the reaction constant of Rxn. 4.4. Substitution of $P_{O_{2,a}}$ into Eq. 4.5 yields

$$E = E^0 - \frac{RT}{2F} ln \frac{P_{H_2O}}{P_{H_2} P_{O_{2,c}}^{\frac{1}{2}}} \tag{4.6}$$

where E^0 is the standard state reversible cell voltage. For example, at room temperature, the product water is in liquid form. The P_{H_2O} term is replaced by activity $a_{H_2O} = 1$. If both H_2 and O_2 are in 1 atm, Eq. 4.6 predicts the open cell voltage (OCV) to be 1.244 V.

Similar to SOFC, the hydrogen permeation membranes operate as a concentration cell. One side of the membrane, the anode side, is fed with high P_{H_2} stream and the other side low P_{H_2} stream. A reversible cell voltage is built across the membrane as a result of the concentration difference

$$E = \frac{RT}{2F} ln \frac{P_{H_{2,h}}}{P_{H_{2,l}}} \tag{4.7}$$

where the subscript h and l represent high and low. Therefore, even if no external circuitry is applied, the separation membrane is still functional, except for the slow kinetics.

In Eq. 4.7, the concentrations are in logarithm terms. Their contribution to voltage is small. For an instance, at room temperature, if $P_{H_{2,h}}$ is 10 orders of magnitude higher than $P_{H_{2,l}}$, the cell voltage is only 0.296 V. At 650 °C , the voltage increases to 0.917 V. In another view, if the atmosphere is identical on both sides, there is still proton flow through the membrane when voltage is applied. From the standpoint of productivity, voltage should be applied in hydrogen separation practice.

4.1.2 Hydrogen Adsorption

H_2 is very small molecule (H-H distance about 0.74 Å) with approximate spherical shape. Due to its small size, the molecule can get very close to a surface in the interaction with solid oxides and metals. Before entering the van der Waals potential field of a solid, the free hydrogen molecule travels at mean thermal velocity of 1800 m/s at room temperature according to Maxwell-Boltzmann distribution. Depending on the incident angle and the solid surface structure, the molecule might be elastically or direct-inelastically scattered without staying long enough to be adsorbed [75].

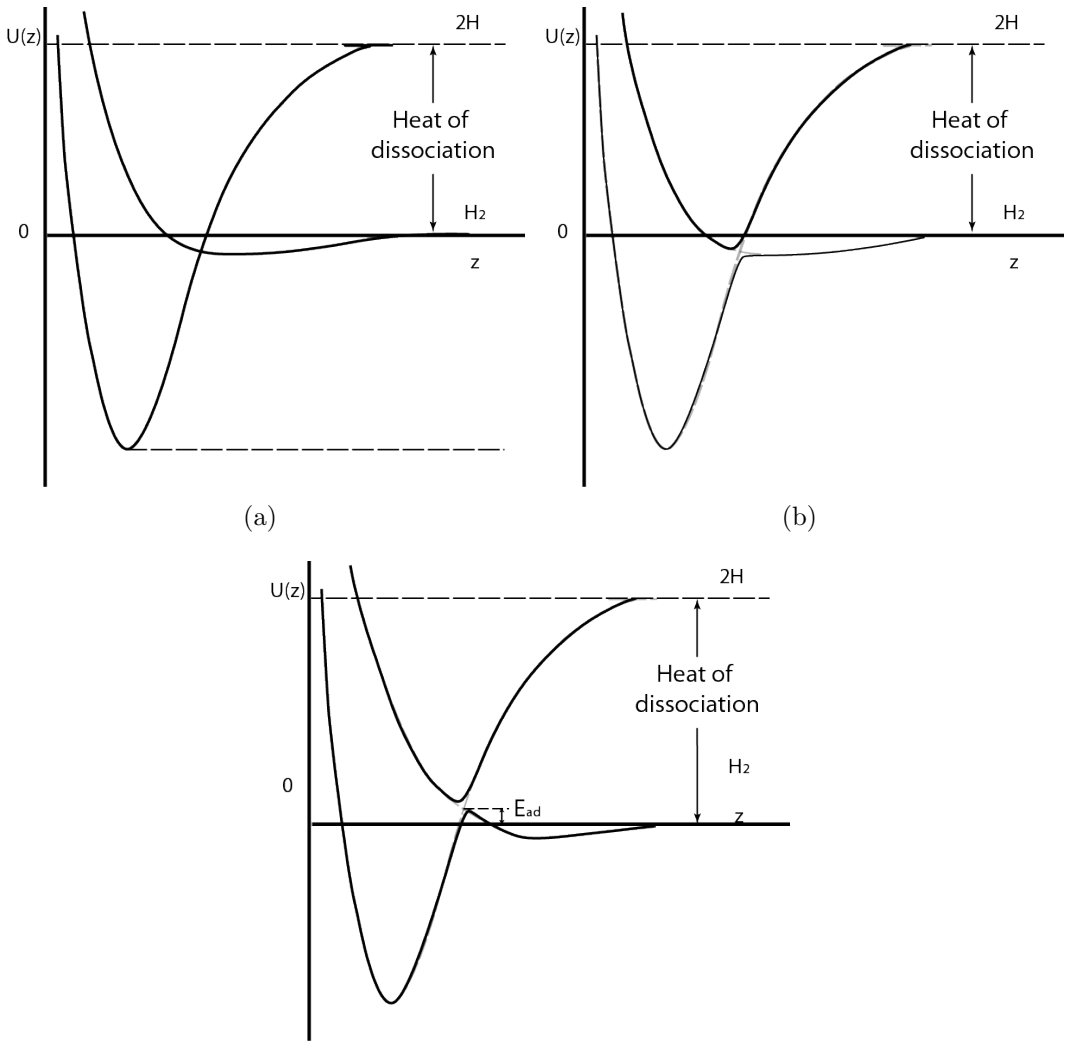

Figure 15: Interaction potential of H_2 with metal reprinted from Ref. [4]

Once trapped, the molecule may stay on the surface transiently before it desorbs or becomes chemisorbed. The initial sticking probability s_0 is defined as the ratio of bound molecules to the colliding ones. The sticking probability beyond zero coverage limit is influenced by the coverage as surface sites are occupied

$$s = s_0(1-\theta)^\alpha \tag{4.8}$$

where θ is the coverage. The power α depends on the adsorption behavior, $\alpha = 1$ for molecule adsorption, and $\alpha = 2$ for dissociative adsorption.

There are two mechanism of chemisorption, spontaneous and activated. Figure 15(a) plots the typical Lennard-Jones potential well as hydrogen molecule approaches the solid and is attracted by the van der Waal force. The other curve represents the dissociated atoms, starting 4.52 eV (436 kJ/mol) above zero, which is the dissociation energy of the hydrogen molecule. Strong interaction between the 1s wave of H atom with the metal leads to steeper potential well. Two curves intercept at a point above or below zero, as depicted in Figure 15(b) and 15(c). In the former case, the dissociation is spontaneous. In the latter case, hydrogen molecule needs to be activated to overcome the barrier of E_{ad}.

The dissociation has two mechanism, too. One is direct dissociation when the translation kinetic energy is sufficient to overcome the energy barrier E_{ad}, if exist. Or alternatively, the molecule has a residence time τ on the surface, staying in precursor state. The precursor is mobile on the surface. Surface defects such as steps can remove the activation barrier and promotes non-activation adsorptions, in systems such as H_2/Ni(111) [76].

Figure 16 shows the surfaces sites on FCC metal. There are atop, hollow and bridge sites. The adsorption energy for different sites are not equal. For example, density function theory (DFT) calculation of H-Pd(100) interaction by Dong et al. gives that the hollow, bridge and top sites have adsorption energy of 0.52 eV, 0.40 eV and -0.08 eV respectively [5]. Adsorbate repulsion is greater for the surfaces with higher concentrations of adatoms in one monolayer.

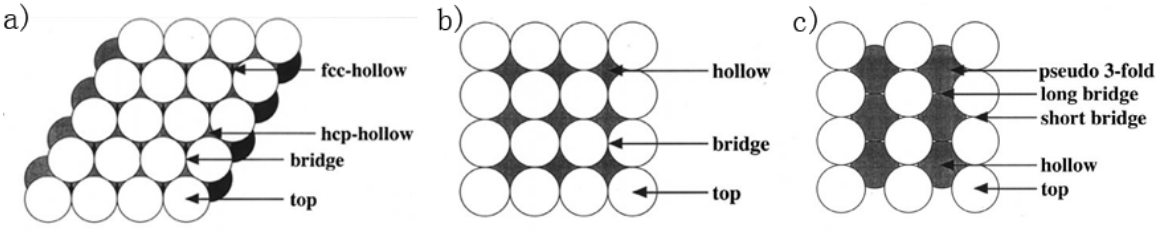

Figure 16: Adsorption sites on FCC metal surface: a). (111), b). (100), and c). (110) [5]

4.2 Elementary Reaction Sequence

At the surface of the metal-BZCYYb cermet membrane, the multistep oxidation of hydrogen can be sequential proton transfer (PT) and electron transfer (ET), or proton-electron coupled transfer process (PCET). Listed in the Table 3 are the possible reaction sequences.

Table 3: Hydrogen oxidization sequences

Concerted electron-proton transfer (EPT)	Electron transferring first	Electron transferring last
$H_2 + s \rightleftharpoons H_{2,ads}$ $H_{2,ads} + s \rightleftharpoons 2H_{ads}$ $H_{ads} + O_O^x \rightleftharpoons OH_{\dot{O}} + e' + s$	$H_2 + s \rightleftharpoons H_{2,ads}$ $H_{2,ads} + s \rightleftharpoons 2H^+ + 2e^{'}$ or $[H_{2,ads} + s \rightleftharpoons 2H_{ads}$ $H_{ads} \rightleftharpoons H^+ + e^{'}]$ $H^+ + O_O^x \rightleftharpoons OH_{\dot{O}} + s$	$H^+ + O_O^x \rightleftharpoons OH_{\dot{O}} + s$ $H_{2,ads} + s \rightleftharpoons 2H_{ads}$ $H_{ads} + O_O^x \rightleftharpoons OH_O + s$ $OH_O \rightleftharpoons OH_{\dot{O}} + e^{'}$

Adopting the PCET assumption, the sequence can be written as follows:

1). Adsorption of a hydrogen molecule on metal surface, taking one surface site

$$H_2 + s \rightleftharpoons H_{2,ads} \tag{4.9}$$

2). Dissociation of the hydrogen molecule into two adsorbed hydrogen atoms

$$H_{2,ads} + s \rightleftharpoons 2H_{ads} \tag{4.10}$$

3). The coupled, or concerted charge and proton transfer in Kroger-Vink notation

$$H_{ads} + O_O^x \rightleftharpoons OH_{\dot{O}} + e' + s \tag{4.11}$$

where s denotes an adsorption site on the metallic catalyst surface. The reaction assumes no moisture in the gas mixture. Figure. 17 illustrates the proposed sequence.

The net rate of a reaction is the difference between forward rate and back rate. The rates of Rxn. 4.9 can be expressed as

$$\vec{r_1} = \vec{k_1} P_{H_2} \Gamma \left(1 - \theta_1 - \theta_2\right) \tag{4.12}$$

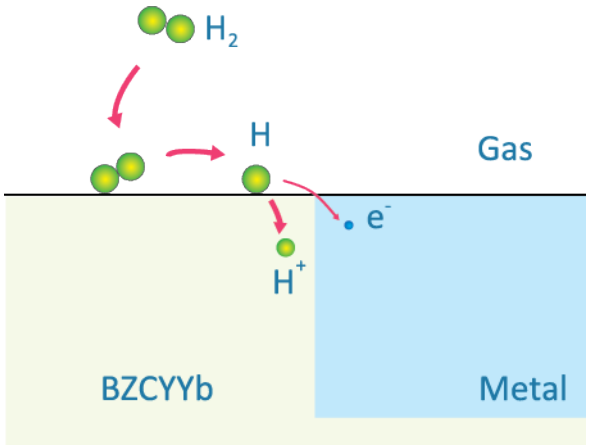

Figure 17: Schematic of the three elementary reaction steps

$$\overleftarrow{r_1} = \overleftarrow{k_1}\Gamma\theta_1 \tag{4.13}$$

where Γ is the number of the surface sites; θ_1 is the fraction of surface sites taken by $H_{2,ads}$ and θ_2 is the fraction taken by H_{ads}. Setting the forward and backward rates to be equal determines the exchange rate constant k_1^0

$$k_1^0 = \overrightarrow{k_1} P_{H_2,0}\Gamma\left(1-\theta_{1,0}-\theta_{2,0}\right) = \overleftarrow{k_1}\Gamma\theta_{1,0} \tag{4.14}$$

where the subscript 0 denotes equilibrium value. The net rate of Rxn. 4.9 can be written in terms of the exchange rate constant

$$r_1 = k_1^0\left[\frac{P_{H_2}\left(1-\theta_1-\theta_2\right)}{P_{H_2,0}\left(1-\theta_{1,0}-\theta_{2,0}\right)} - \frac{\theta_1}{\theta_{1,0}}\right] \tag{4.15}$$

Similarly, for the second step, we have

$$\overrightarrow{r_2} = \overrightarrow{k_2} P_{H_2}\theta_1\Gamma^2\left(1-\theta_1-\theta_2\right) \tag{4.16}$$

$$\overleftarrow{r_2} = \overleftarrow{k_2}(\Gamma\theta_1)^2 \tag{4.17}$$

The rate for the second step, Rxn. 4.10, can be expressed as

$$r_2 = k_2^0\left[\frac{\theta_1(1-\theta_1-\theta_2)}{\theta_{1,0}\left(1-\theta_{1,0}-\theta_{2,0}\right)} - \frac{\theta_2^2}{\theta_{2,0}^2}\right] \tag{4.18}$$

The derivation of the charge transfer kinetics follows the transition state theory and is similar to those in Mebane and Lynch [77–79]. On the energy surface, the reaction

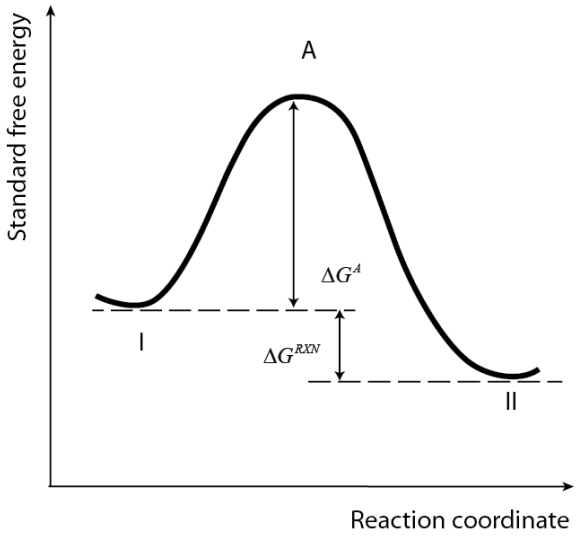

Figure 18: Reaction coordinate diagram

starts from reactant zone I, overcomes potential barrier to activated complex state A, and goes downhill to product zone II, as shown in Figure. 18.

The electrochemical potential of the initial state I/ final state II can be written as a sum of the chemical potentials and electrical potentials of the reactants/ products respectively

$$\bar{\mu}^0_{I,3} = \mu^0_{H_{ads}} + \mu^0_{O^x_O} \tag{4.19}$$

$$\bar{\mu}^0_{II,3} = \mu^0_{OH_O} + \mu^0_e - F\varphi_m + F\varphi_{memb} \tag{4.20}$$

where the subscript m represents the metal phase, and the subscript $memb$ represents the bulk membrane. Introducing transfer coefficient, α, the electrical component of the activated state A can be expressed as

$$\bar{\mu}^0_{A,3} = \mu^0_{A,3} - \alpha F\left(\varphi_m - \varphi_{memb}\right) \tag{4.21}$$

According to transition state theory, the rate constants $\vec{k_3}$ and $\overleftarrow{k_3}$ are calculated by [80]

$$k = \kappa \frac{k_B T}{h} \exp\left(-\frac{\Delta G^0_A}{RT}\right) \tag{4.22}$$

where κ is the transmission coefficient; k_B, h and R are the Boltzmann's constant, Planck's constant and gas constant; ΔG_A^0 is the standard activation energy for state A. Substituting Eqs. 4.19-4.21 into Eq. 4.22 yields

$$\vec{k_3} = \vec{\kappa_3}\frac{k_B T}{h}\exp\left[-\frac{\mu_{A,3}^0 - \left(\mu_{H_{ads}}^0 + \mu_{O_O^x}^0\right) - \alpha F\chi}{RT}\right] \tag{4.23}$$

$$\overleftarrow{k_3} = \overleftarrow{\kappa_3}\frac{k_B T}{h}\exp\left[-\frac{\mu_{A,3}^0 - \left(\mu_{OH_{\dot{O}}}^0 + \mu_e^0\right) - (\alpha-1) F\chi}{RT}\right] \tag{4.24}$$

where $\chi = \varphi_m - \varphi_{memb}$ is the surface potential drop. Again the equilibrium condition determines the exchange rate constant

$$\begin{aligned} k_3^0 &= \vec{\kappa_3}\tfrac{k_B T}{h}\exp\left[-\tfrac{\mu_{A,3}^0 - \left(\mu_{H_{ads}}^0 + \mu_{O_O^x}^0\right) - \alpha F\chi}{RT}\right]\Gamma\theta_{2,0}\gamma_0 \\ &= \overleftarrow{\kappa_3}\tfrac{k_B T}{h}\exp\left[-\tfrac{\mu_{A,3}^0 - \left(\mu_{OH_{\dot{O}}}^0 + \mu_e^0\right) - (\alpha-1) F\chi}{RT}\right]\Gamma\varsigma_0 c_{e,0}\left(1-\theta_{1,0}-\theta_{2,0}\right) \end{aligned} \tag{4.25}$$

where γ is the fraction of O_O^x in O-sites of the membrane, ς is the fraction of $OH_{\dot{O}}$ in O-sites, and c_e is the concentration of electrons in the metal phase.

Eq. 4.25 yields the Bulter-Volmer type rate equation

$$r_3 = k_3^0\left\{\frac{\theta_2\gamma}{\theta_{2,0}\gamma_0}\exp\left(\frac{\alpha F\Delta\chi}{RT}\right) - \frac{\varsigma c_e\left(1-\theta_1-\theta_2\right)}{\varsigma_0 c_{e,0}\left(1-\theta_{1,0}-\theta_{2,0}\right)}\exp\left[-\frac{(1-\alpha) F\Delta\chi}{RT}\right]\right\} \tag{4.26}$$

Here Δ denotes deviation from equilibrium values.

4.3 Cases of Rate Limiting Step

In a multiple-step reaction, if one step is considerably more sluggish than others, that step is called a rate limiting step (RLS). There are three cases with regard to which of the three steps is rate limiting. In each case, the overall reaction rate is determined by the sluggish step, compared with which the other two steps are fast. Fast surface diffusion is also assumed, as high surface diffusivities of hydrogen adatoms on various metals were reported from laser-induced thermal desorption experiments [81–83].

4.3.1 Case I

If the first step is the RLS, the intermediates $H_{2,ads}$ and H_{ads} are present in very low steady-state concentrations. Their rate of formation is virtually balanced by the rate of consumption:

$$\begin{aligned} \theta_1 &\ll 1 \\ \theta_2 &\ll 1 \end{aligned} \tag{4.27}$$

$$\frac{d[H_{2,ads}]}{dt} = \frac{d[H_{ads}]}{dt} = 0 \tag{4.28}$$

The rates of Step 2 & 3 follow the limit of Step 1

$$\begin{aligned} r_2 &= r_1 \\ r_3 &= 2r_1 \end{aligned} \tag{4.29}$$

The overall current density is determined by r_1

$$i_I = 2Fr_1 \tag{4.30}$$

Substituting r_1 from Eq. 4.15

$$i_I = 2F\left[\vec{k_1}P_{H_2}\Gamma\left(1-\theta_1-\theta_2\right) - \overleftarrow{k_1}\Gamma\theta_1\right] \approx 2F\vec{k_1}P_{H_2}\Gamma \tag{4.31}$$

In this case, the current density is proportional to the hydrogen partial pressure

$$i_I \approx 2F\vec{k_1}P_{H_2}\Gamma \propto P_{H_2} \tag{4.32}$$

4.3.2 Case II

If the second step is the RLS, the concentration of $H_{2,ads}$ will be substantial while the concentration of H_{ads} will be very low

$$\theta_2 \ll 1 \tag{4.33}$$

The rates of the Step 1 & 3 are mitigated by the rate of Step 2

$$\begin{aligned} r_1 &= r_2 \\ r_3 &= 2r_2 \end{aligned} \tag{4.34}$$

The current density is determined by r_2

$$i_{II} = 2Fr_2 \approx 2\vec{k_2}F\Gamma^2\theta_1\left(1-\theta_1\right) \tag{4.35}$$

The setting up of the equilibrium of Rxn. 4.9 is fast. Virtually the first step is maintained in equilibrium throughout the process. Assuming Langmuir isothermal behavior, the equilibrium concentration of θ_1 is given by Hill-Langmuir equation

$$\theta_1 = \frac{P_{H_2}K_1}{1+P_{H_2}K_1} \tag{4.36}$$

where K_1 is the reaction constant of Rxn. 4.9. Substitution of θ_1 yields

$$i_{II} = 2\vec{k_2}F\Gamma^2\frac{P_{H_2}K_1}{\left(1+P_{H_2}K_1\right)^2} \tag{4.37}$$

There is no simple order in P_{H_2} but a complex dependence

$$i_{II} \propto \frac{P_{H_2}K_1}{\left(1+P_{H_2}K_1\right)^2} \tag{4.38}$$

4.3.3 Case III

The third step being RLS, the concentrations of both intermediate surface species are considerable. The rates of the Step 1 & 2 are mitigated by the rate of Step 3

$$\begin{aligned} r_1 &= \tfrac{1}{2}r_3 \\ r_2 &= \tfrac{1}{2}r_3 \end{aligned} \tag{4.39}$$

Concentrations of both $H_{2,ads}$ and H_{ads} accumulate close to their equilibrium values in steady state

$$\theta_1 \approx \theta_{1,0} \approx \frac{P_{H_2}K_1}{1+P_{H_2}K_1} \tag{4.40}$$

$$\theta_2 \approx \theta_{2,0} \approx \frac{\left(P_{H_2}K_1K_2\right)^{1/2}}{1+P_{H_2}K_1} \tag{4.41}$$

The current density-overpotential relation

$$i_{III} = k_3^0F\left\{\frac{\gamma}{\gamma_0}\exp\left(\frac{\alpha_3F\eta_1}{RT}\right) - \frac{\varsigma c_e}{\varsigma_0 c_{e,0}}\exp\left[-\frac{\left(1-\alpha_3\right)F\eta_1}{RT}\right]\right\} \tag{4.42}$$

where η_1 is the overpotential across the anode/electrolyte interface. The partial pressure dependence of i_{III} comes from the pre-exponential exchange rate constant k_3^0, which has a pressure dependent factor $\theta_{2,0}$

$$i_{III} \propto \frac{(P_{H_2} K_1 K_2)^{1/2}}{1 + P_{H_2} K_1} \tag{4.43}$$

In summary, the $i - P_{H_2}$ relationship in three cases are listed in Table 4

Table 4: The P_{H_2} dependencies of current density

Cases	Case I	Case II	Case III
Dependencies	$i_I \propto P_{H_2}$	$i_{II} \propto \frac{P_{H_2} K_1}{(1+P_{H_2} K_1)^2}$	$i_{III} \propto \frac{(P_{H_2} K_1 K_2)^{1/2}}{1+P_{H_2} K_1}$

The trends with P_{H_2} are plot in Figure 24

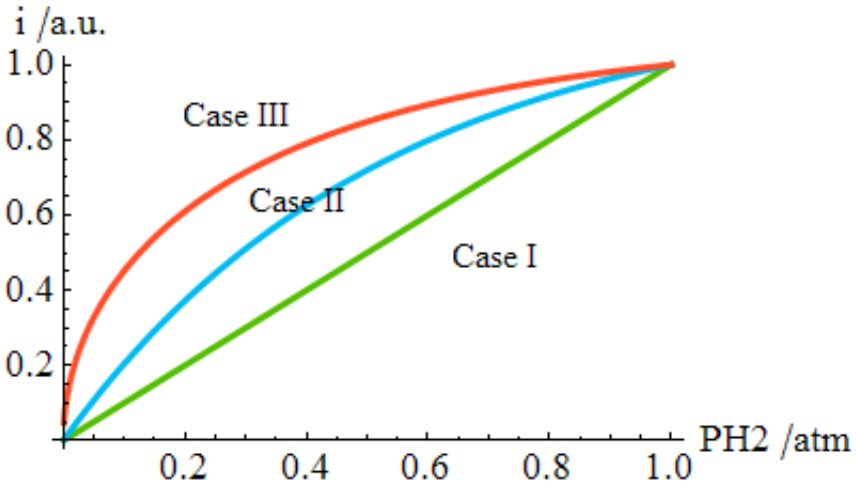

Figure 19: The $i - P_{H_2}$ relation

4.4 The Polarization Resistance at OCV

Besides the $i - P_{H_2}$ dependence, we need another evidence to locate the RLS. As can be seen from analysis of the following chapter, Case I is excluded at first round.

The experimentally available evidence to compare Case II & III is the P_{H_2} dependencies polarization resistance R_p at OCV from electrochemical impedance spectroscopy (EIS)

In Case II, the Step 2 is a chemical reaction. The rate equation Eq. 4.18 does not have explicit potential dependence. In EIS, the applied signal influences r_2 by shifting the equilibrium of Step 3. When a sinusoidal voltage signal Δu is applied to OCV, the resulting current disturbance

$$\Delta i = \Delta \left(2F\vec{k}_2\theta_2^2 \right) \tag{4.44}$$

In two electrode testing set-up, shown in Figure 20, the applied voltage between working and counter consists of three parts

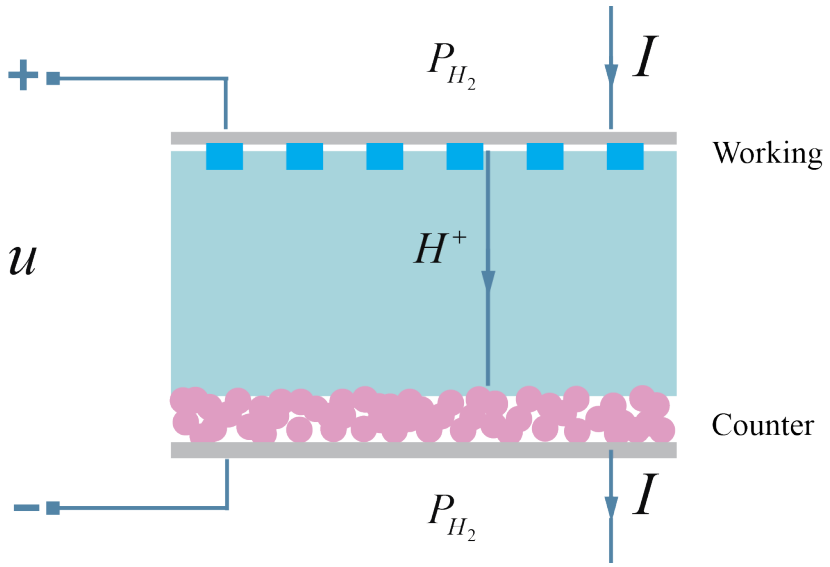

Figure 20: The two electrode testing set-up

$$u = \eta_1 + \eta_2 + \eta_3 \tag{4.45}$$

where η_1, η_2 and η_3 are polarization of working electrode interface, of bulk electrolyte, and of counter electrode interface respectively. When the counter electrode has porous microstructure and much longer TPB length than working, η_3 is negligible compared with η_1 and η_2

$$\eta_2 \ll \eta_1, \eta_3 \tag{4.46}$$

$$U \approx \eta_1 + \eta_2 \tag{4.47}$$

In the small linear region of I-V curve near OCV,

$$\begin{aligned} i &= \tfrac{i_0 F}{RT}\eta_1 \\ i &= \tfrac{1}{AR_{bulk}}\eta_2 \end{aligned} \tag{4.48}$$

where i_0 is the exchange current density, R_{bulk} the bulk resistance of electrolyte and A the effective area of electrolyte. Therefore η_1 and η_2 are also proportional to $u = \Delta u$

$$\begin{aligned} \eta_1 &= \beta_1 \Delta u \\ \eta_2 &= \beta_2 \Delta u \end{aligned} \tag{4.49}$$

β_1 are β_2 proportionality constant. In Case II, the virtual equilibrium of Step 3 gives

$$\theta_2 \approx \theta_{2,0} \exp(-\frac{F}{RT}\eta_1) \tag{4.50}$$

The polarization resistance is defined as

$$R_p^{-1} = \left.\frac{\partial \Delta i}{\partial \Delta u}\right|_{u=0} = C\theta_{2,0}^2 \tag{4.51}$$

Constants were combined into C. The P_{H_2} dependence of R_p

$$R_p^{-1} \propto \frac{P_{H_2}}{\left(1 + P_{H_2} K_1\right)^2} \tag{4.52}$$

In Case III, the P_{H_2} dependence of R_p comes from the term k_3^0 of Eq. 4.26

$$R_p^{-1} = \left.\frac{\partial \Delta i}{\partial \Delta u}\right|_{u=0} = C\theta_{2,0} \tag{4.53}$$

Substituting $\theta_{2,0}$ from Eq. 4.41 we have

$$R_p^{-1} \propto \frac{{P_{H_2}}^{1/2}}{1 + P_{H_2} K_1} \tag{4.54}$$

4.5 Summary

This chapter proposes an elementary reaction sequence of hydrogen oxidation on metal/proton conductor interface, assuming concerted electron and proton transfer.

A kinetic model is developed according to transition state theory. In the simplest case, one step of the sequence limits the overall reaction rate. Three rate limiting cases are discussed. The hydrogen partial pressure dependencies of current density and polarization resistance at OCV are derived to be compared with experiment results. The comparison will test which step is the actual RLS.

CHAPTER V

ELECTROCHEMICAL TESTING AND KINETIC ANALYSIS

5.1 Experimental

$BaZr_{0.1}Ce_{0.7}Y_{0.1}Yb_{0.1}O_{3-\delta}$ powder was synthesized by conventional solid-state reaction method as described in Chapter 2. The test cell is a asymmetric cell. Pt pattern, the working electrode was fabricated by embedding Pt mesh in BZCYYb powder . The powder was dry pressed into green pellets. The pellets were sintered at 1500 °C for 10 h in H_2-Ar (4% H_2) atmosphere, and polished until the mesh was exposed.

The pellets have diameter of 11.5 mm, thickness of 0.5 mm. Porous Pt counter electrode was fabricated on the other side by brush-painting platinum paste onto the pellet and firing at 900 °C for 2 h. The performance of the counter electrode was further enhanced by infiltrating $Pt(NH_3)_4(NO_3)_2$ solution (10 μL, 0.05 mol/L) into the porous microstructure then firing at 750 °C for 1 h. The Pt pattern has a dimension of 5 mm × 5 mm. The asymmetric cell is illustrated in Figure 21.

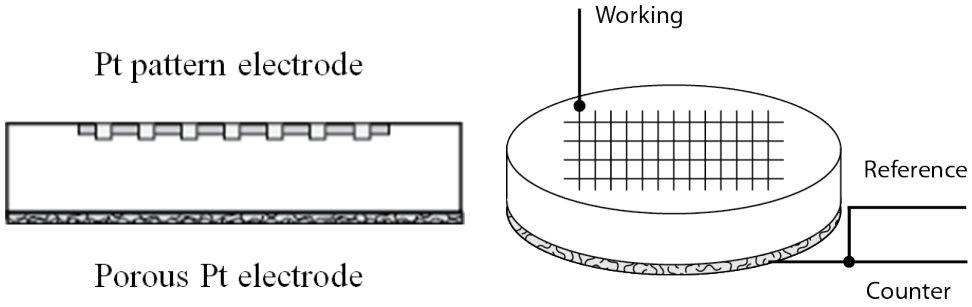

(a) (b)

Figure 21: The asymmetric cell and the two electrode testing configuration

The testing apparatus is illustrated in Figure 22. Hydrogen flow of 50 ml/min flows into the quartz tubes. Both sides of the cell are immersed in identical atmosphere. H_2 flow is balanced by N_2 to change partial pressure of hydrogen from 1 to 0.03. Pt mesh was used as current collector and was pressed against the electrodes by strings.

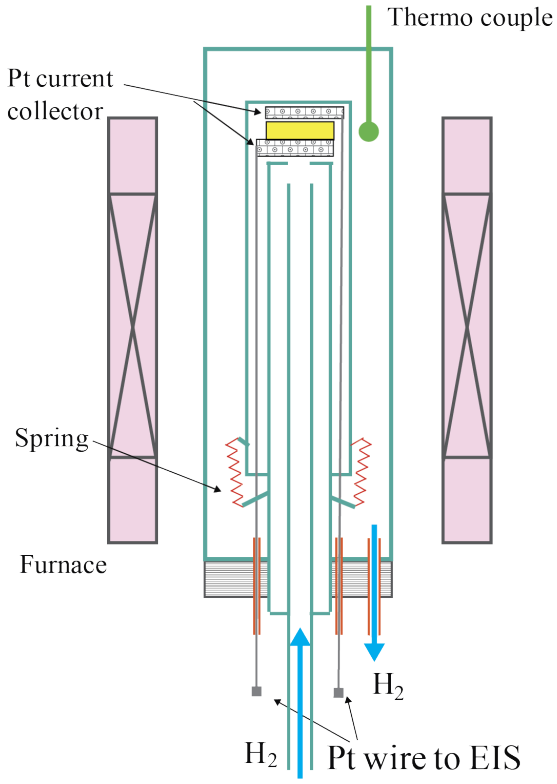

Figure 22: Schematic of the electrochemical testing system

The impedance measurement at each hydrogen partial pressure is acquired by an EGG potentiostat coupled with Solartron frequency response analyzer. Frequency swept from 100 kHz to 0.1 Hz, with AC signal amplitude of 10 mV. The cell is polarized from OCV to 0.5 V, 0.1V per step, to acquire the steady-state current.

5.2 Result Analysis

A thermally assisted field emission SEM Leo 1530 was used to characterize the morphology of the Pt pattern electrode and the Pt porous counter electrode.

Figure 23(a) shows the surface view of the pattern electrode and the electrolyte.

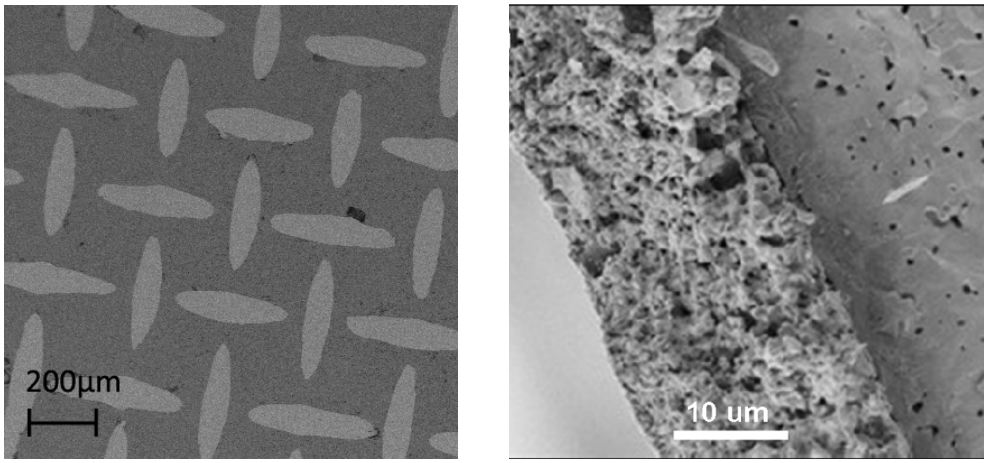

(a) (b)

Figure 23: The morphologies of the (a). Pt pattern electrode and (b). Pt porous counter electrode

The dark grey part is BZCYYb electrolyte, while the light grey part is Pt pattern. They display good contact and clear edge. Figure 23(b) shows that the Pt counter electrode has porous microstructure of $\sim$30 μm thick. The Pt particle has diameter of $\sim$2 μm. They form connected network instead of agglomerated metal chunk.

At 550 °C, the Pt porous electrode with 0.5wt% Pt infiltration has area specific resistance of 0.45 Ωcm^2, which is two orders of magnitude smaller that of working electrode. We are confident in neglecting the overpotential of counter electrode

$$\eta_1 \approx u - \eta_2 = u - IR_{Ohm} \tag{5.1}$$

The overpotential over working electrode is the applied voltage minus the Ohmic potential drop IR_{Ohm} across the electrolyte, including Ohmic contact resistance of the electrode/electrolyte interfaces. R_{Ohm} is read from the high frequency intercept of the impedance spectroscopy.

Figure 24 shows the $I - P_{H_2}$ relation under different bias. Subtracting the Ohmic drop from the applied voltage, the $I - \eta$ relation is plot in Figure 25.

Shown in Figure 26 is typical semi-circle impedance spectra under different P_{H_2}. For each semi-circle, the Ohmic resistance R_{Ohm} reflects the contribution of bulk

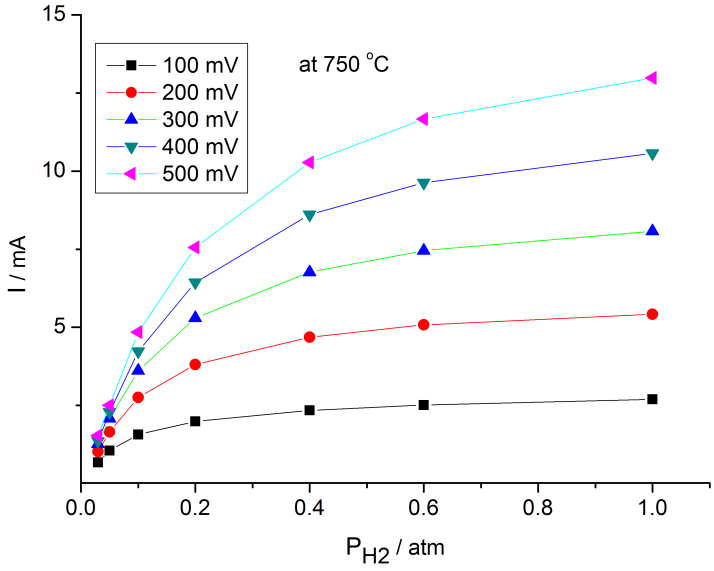

Figure 24: The $I - P_{H_2}$ curve under different applied voltage at 750 °C

electrolyte and contact resistance. R_{Ohm} is the intercept with the real axis at high frequency end. The polarization resistance R_p is associated with the diffusion and electrochemical process of the electrode. R_p is calculated by the difference between the two intercepts with the real axis at high and low frequencies. Both R_{Ohm} and R_p increase with decreasing hydrogen partial pressure. The two arches split as P_{H_2} decreases.

Figure 27 shows the R_p relation at different temperatures. R_p is not sensitive to P_{H_2} when hydrogen supply is sufficient. When P_{H_2} drops below 50%, the hydrogen hunger is reflected by the steep rise of R_p.

5.3 Rate Limiting Case Fitting

5.3.1 $i - P_{H_2}$ relation

To study the effect of P_{H_2} on current density, the overpotential on the working electrode must be fixed. Two overpotentials were chosen: 50 mV and 180 mV. They represent the scenarios of low and higher polarization. Intercept Figure 25 with

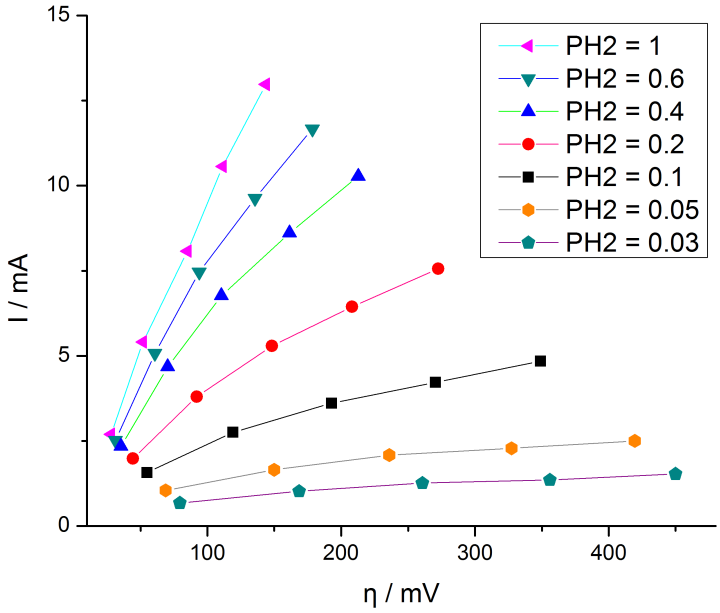

Figure 25: The $I - \eta$ curve under different P_{H_2} at 750 °C

two vertical lines $\eta = 50\text{mV}$ and $\eta = 180\text{mV}$, we get $i - P_{H_2}$ curve under fixed overpotential. Fitting the curves into the three models are listed in Table 4, the results are plot in Figure 28.

Figure 28(a) and 28(b) compares the three case models. The experimental data is marked by open triangles. Apparently Case I is excluded since the data deviate faraway from linear behavior. Case II is the most fit to the both data sets. Take

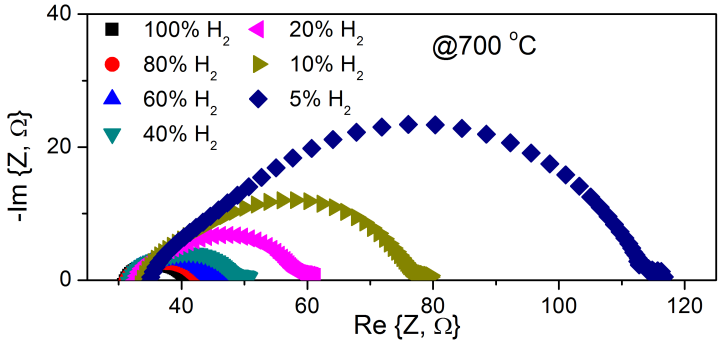

Figure 26: The impedance spectra under different P_{H_2} at 700 °C

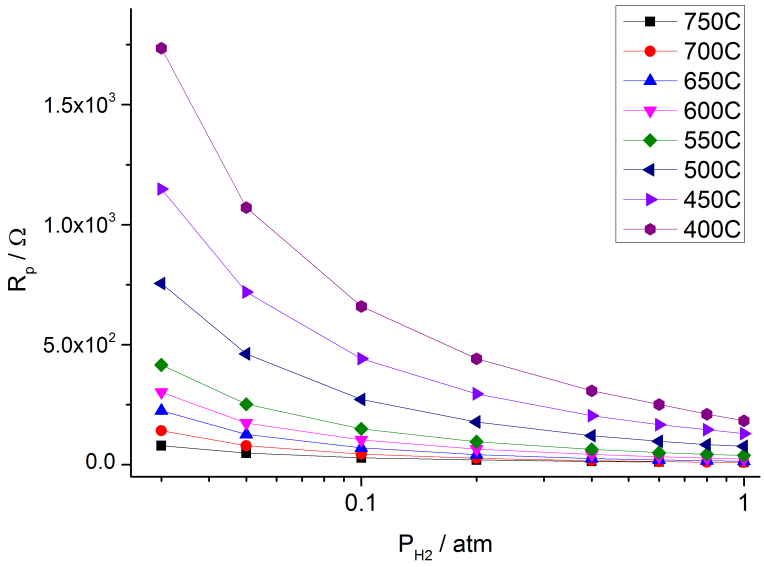

Figure 27: The P_{H_2} dependence of polarization resistance under different temperatures

an closer look of Case II and III in logarithm scale. As seen from Figure 28(c) and 28(d), Case II fits better into the experimental data than Case III, especially at higher polarization. Case III has a positive intercept with vertical axis as P_{H_2} moves closer to zero. In contrast, in Case II the fitted I approximates zero as P_{H_2} is close to zero. Since the rate of the charge transfer step increases exponentially with polarization in the activation-limited region, it is possible that Case III is rate limiting or co-rate-limiting at low polarization and stops limiting reaction rate when polarization increases.

The fitted parameters of Case II and III are listed in Table 5.

C_1 is a lumped proportionality term. The parameter of interest is K_1. Case III returns the reaction constant K_1 close to zero in the order of 10^{-11}. In this case, the $i - P_{H_2}$ relation degenerates to

$$i_{III} \propto \frac{C_1 {P_{H_2}}^{1/2}}{1 + P_{H_2} K_1} \approx P_{H_2}^{1/2} \tag{5.2}$$

in which case the reaction order with respect to P_{H_2} is 1/2. However, in deriving

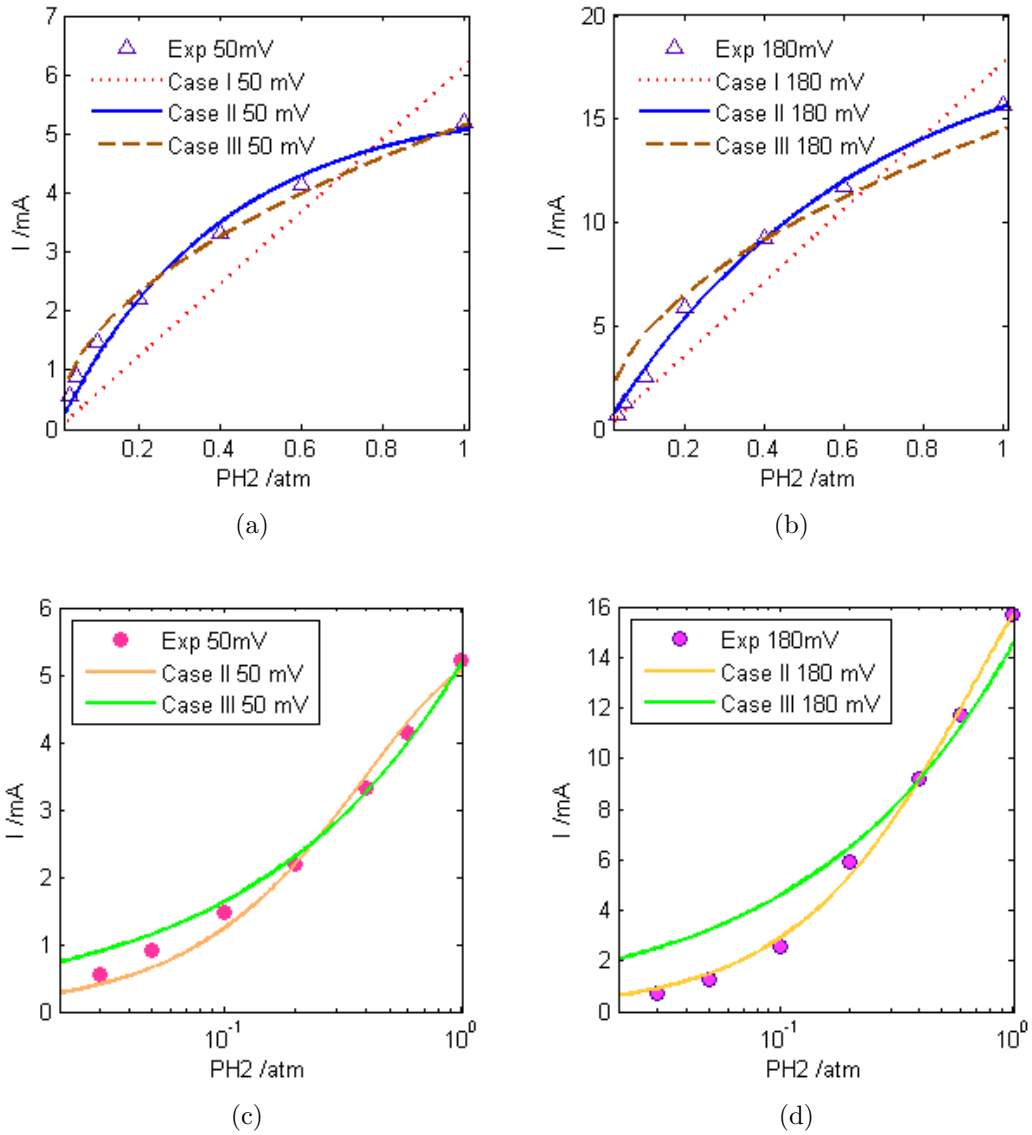

Figure 28: Model fitting of $i - P_{H_2}$ curves

Table 5: Parameters from model fitting

Case **Overpotential**	**Case II** $\mathrm{i}_{II} \propto \frac{C_1 P_{H_2}}{\left(1+P_{H_2}K_1\right)^2}$	**Case III** $\mathrm{i}_{III} \propto \frac{C_1 {P_{H_2}}^{1/2}}{1+P_{H_2}K_1}$
50 mV	$C_1 = 13.98$ $K_1 = 0.6625$	$C_1 = 5.151$ $K_1 = 6.542\text{E-}11$
180 mV	$C_1 = 31.23$ $K_1 = 0.4149$	$C_1 = 14.48$ $K_1 = 2.829\text{E-}11$

Eq. 4.40 and 4.41 K_1 is assumed to be substantially larger than K_2. The trivial K_1 corresponds to the mechanism of direct-dissociation. Namely, H_2 from gas phase directly dissociates into atoms upon chemical adsorption, without going through $H_{2,ads}$ precursor stage. The direct-dissociation is discussed in Section. 5.4.1.

Case III returns parameter contradicting with the presupposition of the derivation. Therefore it is a false fit. In contrast, Case II returning K_1 around 0.5. For hydrogen pressure at 1 atm, $K_1 = 0.5$ yields coverage of 0.33.

To summarize the fitting of $i - P_{H_2}$ curve, we have

i). Case II fits well for both $\eta_1 = 50mV$ and $\eta_1 = 180mV$.

ii). Case II returns non-trivial reaction constant K_1 at 750 °C.

iii). Case III does not fit well with $\eta = 180mV$. In both fitting of $\eta = 50mV$ and $\eta = 180mV$, the fitted curve has considerable positive ($1 \sim 2$ mA) intercepts with the current axis.

iv). Case III fitting contradicts the non-dissociative-adsorption premise of the model, therefore is not valid.

The preliminary conclusion is that Case II is the most probable case. To confirm the conclusion, more evidence is needed from examination of electrochemical behavior at OCV.

5.3.2 The Polarization Resistance at OCV

The EIS test results are shown in Figure 26 and 27. The models to be fitted are Eq. 4.52 and 4.54.

Figure 29 shows the fitting result of 650 °C and 700 °C. Case II fits perfectly for both temperatures, while Case III fails to fit either of them.

In fact, Case II successfully fits the data of full temperature spectrum, as shown in Figure 30.

The fitted parameters are summarized in Table 6. Again, Case III returns K_1 close to zero, the P_{H_2} dependence degenerates to $R_p \propto P_{H_2}^{1/2}$.

Table 6: Parameters from model fitting

Case **Temperature**	**Case II** $R_p \propto \frac{C_1(1+PK_1)^2}{P}$	**Case III** $R_p \propto \frac{C_1(1+PK_1)}{P^{1/2}}$
750 °C	$C_1 = 2.200$ $K_1 = 1.335$	$C_1 = 11.71$ $K_1 = 3.881\text{E-}10$
700 °C	$C_1 = 4.006$ $K_1 = 0.6135$	$C_1 = 19.26$ $K_1 = 2.031\text{E-}11$
650 °C	$C_1 = 6.386$ $K_1 = 0.5635$	$C_1 = 30.52$ $K_1 = 2.047\text{E-}08$
600 °C	$C_1 = 8.496$ $K_1 = 0.8541$	$C_1 = 42.29$ $K_1 = 2.087\text{E-}09$
550 °C	$C_1 = 11.75$ $K_1 = 1.003$	$C_1 = 59.79$ $K_1 = 2.318\text{E-}12$
500 °C	$C_1 = 21.28$ $K_1 = 1.078$	$C_1 = 109.4$ $K_1 = 4.748\text{E-}12$
450 °C	$C_1 = 32.35$ $K_1 = 1.246$	$C_1 = 170.5$ $K_1 = 2.785\text{E-}11$
400 °C	$C_1 = 48.77$ $K_1 = 1.209$	$C_1 = 255.7$ $K_1 = 1.715\text{E-}09$

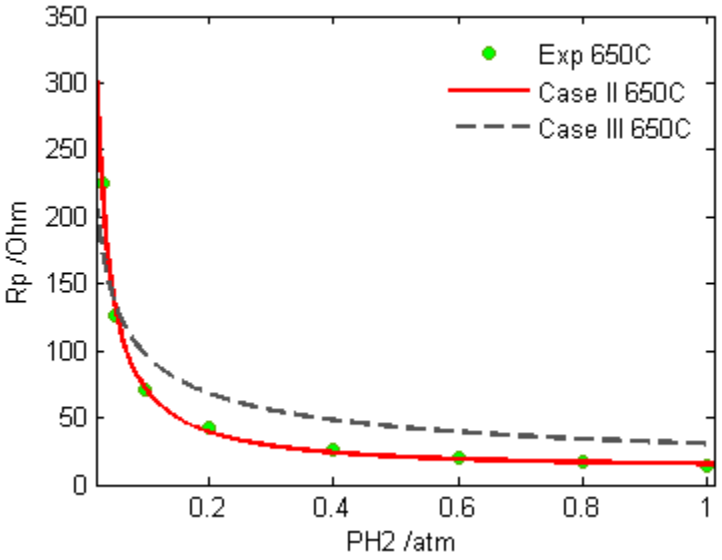

(a)

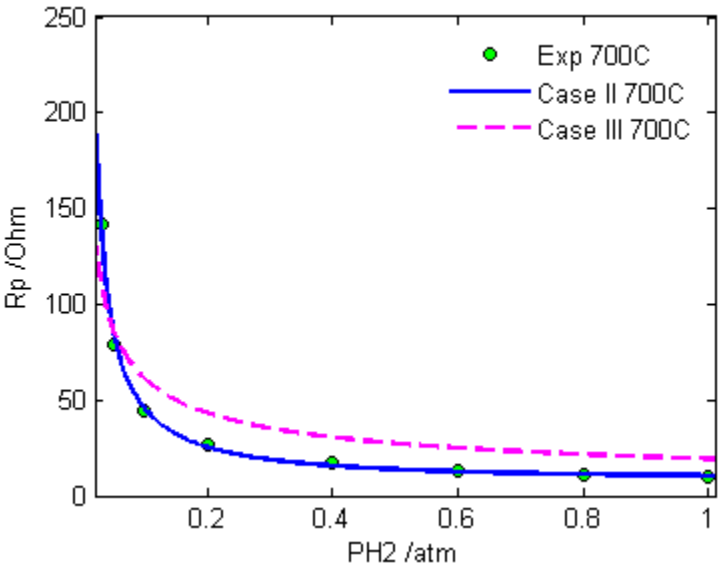

(b)

Figure 29: Model fitting of $R_p - P_{H_2}$ curves

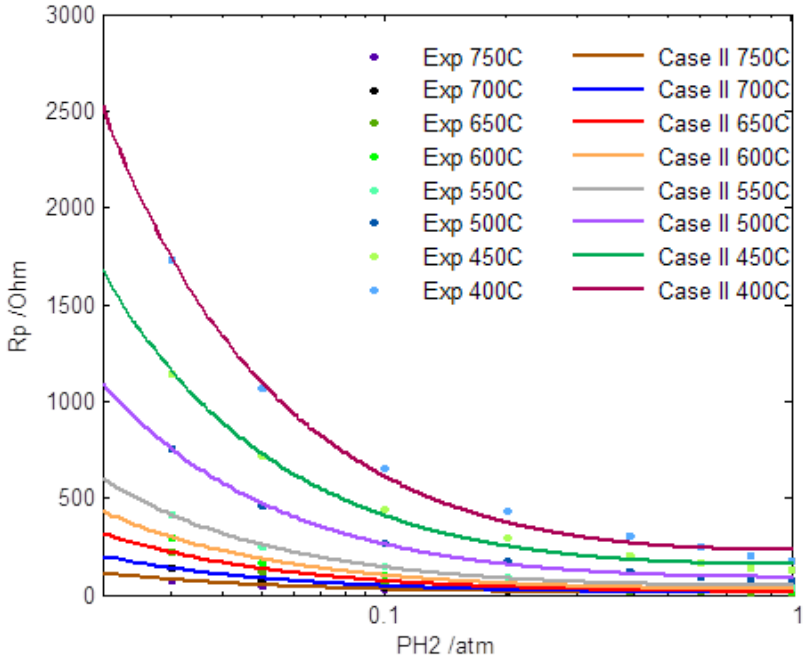

Figure 30: Case II fitting of R_p at all temperatures

As seen from Table 6, Case II displays high self-consistency. K_1 of Case II falls in the same order of 0.5∼1. In contrast, K_1 of Case III is bouncing between orders of magnitude.

Therefore, evidences from polarization resistance dependence reinforces the conclusion that Case II is the most probable case:

i). Case II fits perfectly with experimental data, while Case III fails to fit;

ii). Parameters of Case II are highly self-consistent, while parameters of Case III are not in agreement with each other.

5.4 Discussion

5.4.1 Direct Dissociation

Adsorption of hydrogen on Ni is probably dissociative [84]. When $K_1 \ll K_2$, the two-step adsorption collapses to one dissociative adsorption, too, referred here as Step

2'

$$H_2 + 2s \rightleftharpoons 2H_{ads} \tag{5.3}$$

in which case the equilibrium coverage of adatom is given by

$$\theta' = \frac{\sqrt{KP} - KP}{1 - KP} \tag{5.4}$$

K is the equilibrium constant $K = K_1 K_2$. Substituting $\frac{\theta_1}{\theta_2}$ with θ' in P_{H_2} dependence equations and do the fitting, neither Case II or Case III fits into the experimental data. The direct dissociation hypothesis is not compatible with this kinetic model.

5.4.2 Step 2 and 3 Co-limiting

Developing the kinetic model assumes limit situation, one step significantly more sluggish than the others. It is possible in the real world the reaction is co-limited by multiple factors. The rate of Step 3 increases exponentially with polarization before reaching the diffusion-limited plateau. In contrast, Step 2 is a chemical reaction. The rate of Step 2 is indirectly influenced by potential via shift of equilibrium. When the bias is low and P_{H_2} is high, it is possible that both Step 2 and 3 will contribute to the limiting rates. However, Figure 31 shows that for $P_{H_2} = 0.5$, the low frequency arch

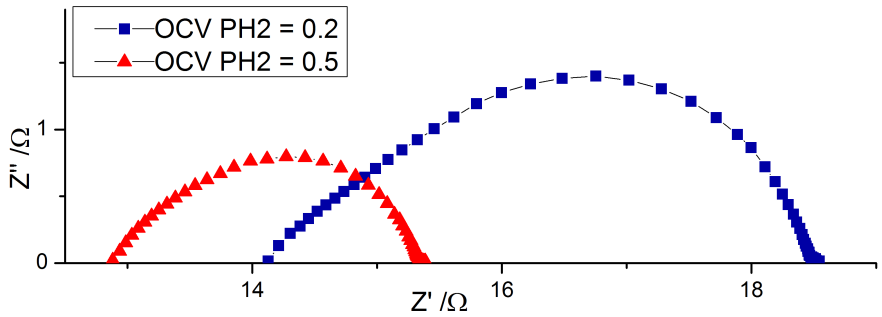

Figure 31: Impedance spectroscopy of Pd pattern electrode at OCV

is dominating even at OCV. In the equivalent circuits as shown in Figure 32, R1 = 0.42 Ω < R2 = 3.80 Ω for $P_{H_2} = 0.2$; R1 = 0.12 Ω < R2 = 2.27 Ω for $P_{H_2} = 0.5$. The charge transfer is not rate limiting near OCV. Syngas typically has 20∼40vol% of

hydrogen. Jiang observed the similar phenomena of $R_H > R_L$ in Ni/GDC electrode. The ratio of $\frac{R_H}{R_L}$ is increasing with decreasing temperature [85]. In SOFC and hydrogen permeation membrane operating conditions, there is bias applied. The contribution of charge transfer should be much smaller compared to OCV.

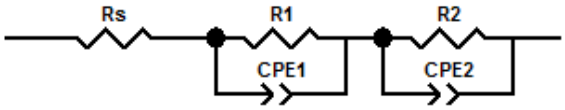

Figure 32: Equivalent circuits of the metal/proton conductor interface

5.4.3 Comparison with Literature

Water content may play an important role in the hydrogen oxidation. In systems such as Ni/YSZ, increasing water vapor up to a certain amount in the gas mixture will boost the reaction and reduce the impedance, especially the low frequency arc [33,86]. To account for the water vapor effect Jiang proposed a spill-over mechanism. H_2O molecules will form $O-S$ and subsequently $H_{ads}-O-S$ with the metal surface sites S. The surface transport is accelerated via the fast surface diffusion of $H_{ads}-O-S$, which explains the low frequency impedance shrink [29]. The water mediated spill-over mechanism only applies to metals with low oxide formation Gibbs free energy like Ni and Pd [29,85].

In Pt/BZCYYb system, the performance is insensitive to water vapor content as shown in Figure 33(a) [87]. The observation agrees with the central conclusion in that the reaction is not limited surface diffusion. Akoshima found similar insensitivity of porous Pt electrode on proton conductor BCY [40]. Instead the electrode interfacial conductivity σ_E is strongly determined by hydrogen partial pressure. Akoshima analyzed that $\sigma_E \propto P_{H_2}^{\beta}$, $\beta = 0.75$ and 0.5 for 600 °C and 500 °C respectively. The model of this work predicts the general dependence of $\sigma_E \propto \frac{P_{H_2}}{(1+P_{H_2}K_1)^2}$ as derived in Eq. 4.52.

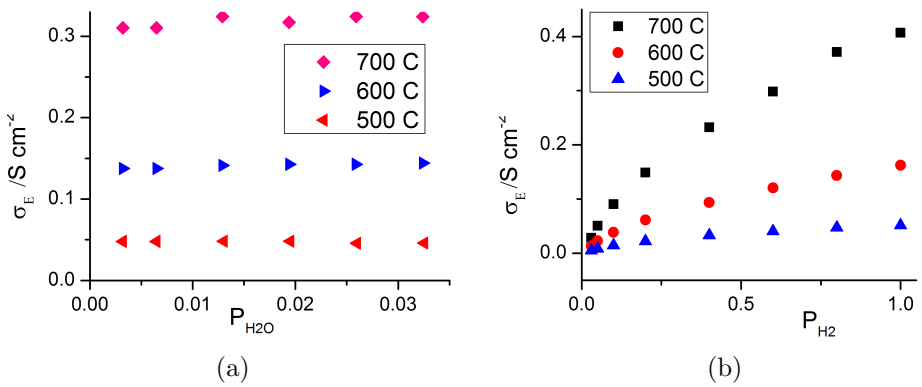

Figure 33: Electrode interfacial conductivity at different a). P_{H_2O} and b). P_{H_2}

In literature, surface diffusion was suggested to be possible rate limiting process for both metal/oxygen conductor [72,85] and metal/proton conductor systems [36,40]. To derive analytical dependence, the kinetic model of this work assumes fast surface diffusion, as hydrogen atom was proved to highly mobile on metal surfaces. DFT calculated that the hydrogen diffusion barrier on the (111) surface of a variety of metals falls into the small range of $0.06 \sim 0.15$ eV, including Pt, Pd, Au, Ag, Ir, Cu and Ni [88]. Experimental evidences support that the activation energy for hydrogen transport on metal surfaces is small [82, 83]. the In continued development of the kinetic model, surface diffusion can be taken into consideration in numerical model.

CHAPTER VI

CONCLUSION AND RECOMMENDATIONS

This work presents the analysis of the reaction rates of the proposed pathway and predicts the performance given one of the step is rate limiting. Accordingly, electrochemical tests were designed to validate the predictions of different cases. Both the current density and polarization resistance dependencies on partial pressure of hydrogen suggest the dissociation of hydrogen is the RLS. The quantitative agreement of the model with experiments unambiguously supports the proposed reaction sequence and the PCET assumption. Based on the kinetic model, following future work is recommended.

For experiments, the electrochemical tests are to be repeated on different metal catalyst candidates, Pd, Ni, Co etc. To compare the catalytic activities, pattern electrode fabrication by photolithography is the best choice. The kinetic activities of the metals are to be normalized by TPB length and compared. The resulting length specific pre-exponential parameter provides input for simulation work.

For modeling, the kinetic model is to be adapted into a numerical model of 1D, 2D or 3D geometry. 1D model compares the relative contribution of Step 2 and 3 in the co-limiting case. Starting from 2D, the surface diffusion can be taken into consideration. 2D model is adequate to simulate pattern electrode performance, while 3D model is able to simulate electrode of arbitrary microstructure, following the conformal modeling method developed by Lynch [89].

The combination of the experiment and modeling shall provide insights in the engineering of the material property and the optimization of the electrode architecture for SOFC, hydrogen permeation membranes, and other electrochemical devices.

REFERENCES

[1] T. Ishihara. *Perovskite Oxide for Solid Oxide Fuel Cells*. Fuel cells and hydrogen energy. Springer London, Limited, 2009.

[2] K. D. Kreuer. Proton-conducting oxides. *Annual Review of Materials Research*, 33:333–359, 2003.

[3] M. L. Liu, L. Yang, S. Z. Wang, K. Blinn, M. F. Liu, Z. Liu, and Z. Cheng.

[4] K. Christmann. Interaction of hydrogen with solid surfaces. *Surface Science Reports*, 9(13):1–163, 1988.

[5] W. Dong, V. Ledentu, Ph. Sautet, A. Eichler, and J. Hafner. Hydrogen adsorption on palladium: a comparative theoretical study of different surfaces. *Surface Science*, 411(12):123 – 136, 1998.

[6] The World Bank. World Development Indicators. page 168, 2012.

[7] International Energy Agency. World Energy Outlook 2012. page 5, 2012.

[8] U.S. Energy Information Administration. Annual Energy Outlook 2012, with Projections to 2035. pages 3, 24, 2012.

[9] K. T. Adjemian, S. J. Lee, S. Srinivasan, J. Benziger, and A. B. Bocarsly. Silicon oxide nafion composite membranes for proton-exchange membrane fuel cell operation at 80-140c. 149(3):A256–A261, 2002.

[10] K.D. Kreuer. *Fuel Cells*. Springer, 2012.

[11] LatifahA. Adams, SimonD. Poynton, Christelle Tamain, RobertC.T. Slade, and JohnR. Varcoe. A carbon dioxide tolerant aqueous-electrolyte-free anion-exchange membrane alkaline fuel cell. *ChemSusChem*, 1(1-2):79–81, 2008.

[12] N.Q. Minh and T. Takahashi. *Science and Technology of Ceramic Fuel Cells*. Elsevier Science, 1995.

[13] Mogens Mogensen, Nigel M. Sammes, and Geoff A. Tompsett. Physical, chemical and electrochemical properties of pure and doped ceria. *Solid State Ionics*, 129(14):63 – 94, 2000.

[14] N. Sammes and Y. Du. *Intermediate-Temperature SOFC Electrolytes*, volume 202 of *NATO Science Series*, chapter 3, pages 19–34. Springer Netherlands, 2005.

[15] S. B. Adler. Factors governing oxygen reduction in solid oxide fuel cell cathodes. *Chemical Reviews*, 104(10):4791–4843, 2004.

[16] Yoshio Matsuzaki and Isamu Yasuda. Dependence of sofc cathode degradation by chromium-containing alloy on compositions of electrodes and electrolytes. *Journal of The Electrochemical Society*, 148(2):126–131, 2001.

[17] Naoki Ito, Masahiko Iijima, Kenji Kimura, and Satoshi Iguchi. New intermediate temperature fuel cell with ultra-thin proton conductor electrolyte. *Journal of Power Sources*, 152(0):200 – 203, 2005.

[18] R.D. Noble and S.A. Stern. *Membrane Separations Technology: Principles and Applications*. Membrane Science and Technology. Elsevier Science, 1995.

[19] S.C.A. Kluiters. Status Review on Membrane Systems for Hydrogen Separation. *Energy Research Centre of the Netherlands: Petten, The Netherlands*, page 168, 2004.

[20] J. R. Young. Purity of Hydrogen Permeating through Pd, Pd-25(Ag, and Ni. *Review of Scientific Instruments*, 34(8):891–, 1963.

[21] Sushil Adhikari and Sandun Fernando. Hydrogen membrane separation techniques. *Industrial Engineering Chemistry Research*, 45(3):875–881, 2006.

[22] U Balachandran, B Ma, P.S Maiya, R.L Mieville, J.T Dusek, J.J Picciolo, J Guan, S.E Dorris, and M Liu. Development of mixed-conducting oxides for gas separation. *Solid State Ionics*, 108(14):363 – 370, 1998.

[23] U. Balachandran, T. H. Lee, G. Zhang S. Wang, J. J. Picciolo, J. T. Dusek, and S. E.Dorris. Recent advances in the development of dense ceramic membranes for hydrogen separation. *Energy Technology Division, Argonne National Laboratory*, 47(2):820, 2002.

[24] H. Iwahara, Y. Asakura, K. Katahira, and M. Tanaka. Prospect of hydrogen technology using proton-conducting ceramics. *Solid State Ionics*, 168(3-4):299–310, 2004.

[25] K. Katahira, Y. Kohchi, T. Shimura, and H. Iwahara. Protonic conduction in Zr-substituted BaCeO3. *Solid State Ionics*, 138(1-2):91–98, 2000.

[26] K. H. Ryu and S. M. Haile. Chemical stability and proton conductivity of doped BaCeO3-BaZrO3 solid solutions. *Solid State Ionics*, 125(1-4):355–367, 1999.

[27] Ben H. Rainwater, Mingfei Liu, and Meilin Liu. A more efficient anode microstructure for SOFCs based on proton conductors. *International Journal of Hydrogen Energy*, 37(23):18342 – 18348, 2012.

[28] Changcheng Chen, Mingfei Liu, Yaohui Bai, Lei Yang, Erqing Xie, and Meilin Liu. Anode-supported tubular SOFCs based on BaZr0.1Ce0.7Y0.1Yb0.1O3-δ electrolyte fabricated by dip coating. *Electrochemistry Communications*, 13(6):615 – 618, 2011.

[29] S. P. Jiang and S. P. S. Badwal. Hydrogen oxidation at the nickel and platinum electrodes on yttria-tetragonal zirconia electrolyte. *Journal of The Electrochemical Society*, 144(11):3777–3784, 1997.

[30] Wolfgang G. Bessler, Marcel Vogler, Heike Stormer, Dagmar Gerthsen, Annika Utz, Andre Weber, and Ellen Ivers-Tiffee. Model anodes and anode models for understanding the mechanism of hydrogen oxidation in solid oxide fuel cells. *Physical Chemistry Chemical Physics*, 12(42):13888–13903, 2010.

[31] A Ringued, D Bronine, and J.R Frade. Assessment of Ni/YSZ anodes prepared by combustion synthesis. *Solid State Ionics*, 146:219 – 224, 2002.

[32] S. Primdahl and M. Mogensen. Oxidation of Hydrogen on Ni/Yttria Stabilized Zirconia Cermet Anodes. *Journal of The Electrochemical Society*, 144(10):3409–3419, 1997.

[33] Junichiro Mizusaki, Hiroaki Tagawa, Takatoshi Saito, Tamaki Yamamura, Kouji Kamitani, Katsuhiko Hirano, Shaw Ehara, Toshinori Takagi, Tomoji Hikita, Masamichi Ippommatsu, Shigeto Nakagawa, and Keiichi Hashimoto. Kinetic studies of the reaction at the nickel pattern electrode on YSZ in H2H2O atmospheres, journal = Solid State Ionics. 7071, Part 1(0):52–58, 1994.

[34] A. Bieberle, L. P. Meier, and L. J. Gauckler. The electrochemistry of Ni pattern anodes used as solid oxide fuel cell model electrodes, journal = Journal of the Electrochemical Society. 148(6):A646–A656, 2001.

[35] S. B. Adler and W. G. Bessler. *Elementary kinetic modeling of solid oxide fuel cell electrode reactions*. John Wiley Sons, Ltd, 2010.

[36] Darja Kek, Nikolaos Bonanos, Mogens Mogensen, and Stane Pejovnik. Effect of electrode material on the oxidation of H2 at the metal-Sr0.995Ce0.95Y0.05O2.970 interface. *Solid State Ionics*, 131(34):249 – 259, 2000.

[37] D Kek and N Bonanos. Electrochemical H-D isotope effect at metalperovskite proton conductor interfaces. *Solid State Ionics*, 125(14):345 – 353, 1999.

[38] Darja Kek and Nikolaos Bonanos. Investigation of hydrogen oxidation reaction on a metal/perovskite proton conductor interface by impedance spectroscopy. *Vacuum*, 61:453 – 457, 2001. Proceedings of the 8th joint Vaccum Conference of Croatia, Austria, Slovenia and Hungary.

[39] S. Zisekas, G. Karagiannakis, and M. Stoukides. Electrode polarization at the Pd/proton conductor interface. *Solid State Ionics*, 176(3940):2929 – 2934, 2005.

Selected Papers from the 12th International Conference on Solid State Proton Conductors (SSPC-12).

[40] Satoshi Akoshima, Masatsugu Oishi, Keiji Yashiro, Kazuhisa Sato, and Junichiro Mizusaki. Reaction kinetics on platinum electrode / yttrium-doped barium cerate interface under H2-H2O atmosphere. *Solid State Ionics*, 181:240 – 248, 2010. 14th International Conference on Solid State Protonic Conductors, Kyoto, Japan, 7-11 September 2008.

[41] Benjamin Auer, Laura E. Fernandez, and Sharon Hammes-Schiffer. Theoretical Analysis of Proton Relays in Electrochemical Proton-Coupled Electron Transfer. *Journal of the American Chemical Society*, 133(21):8282–8292, 2011.

[42] D. Perednis and L. J. Gauckler. Solid oxide fuel cells with YSZ films prepared using spray pyrolysis. *Solid Oxide Fuel Cells Viii (Sofc Viii)*, 2003(7):970–975, 2003.

[43] C.C. Chen, M.M. Nasrallah, and H.U. Anderson. Synthesis and characterization of ysz thin film electrolytes. *Solid State Ionics*, 7071, Part 1(0):101 – 108, 1994.

[44] Jennifer L.M. Rupp and Ludwig J. Gauckler. Microstructures and electrical conductivity of nanocrystalline ceria-based thin films. *Solid State Ionics*, 177(2632):2513 – 2518, 2006.

[45] Toshio Suzuki, Igor Kosacki, and Harlan U Anderson. Microstructureelectrical conductivity relationships in nanocrystalline ceria thin films. *Solid State Ionics*, 151(14):111 – 121, 2002. Proceedings of the Second International Symposium on Soft Solution Processing 2000.

[46] James Wright and Anil V. Virkar. Conductivity of porous sm2o3-doped ceo2 as a function of temperature and oxygen partial pressure. *Journal of Power Sources*, 196(15):6118 – 6124, 2011.

[47] K.D. Kreuer, St. Adams, W. Munch, A. Fuchs, U. Klock, and J. Maier. Proton conducting alkaline earth zirconates and titanates for high drain electrochemical applications. *Solid State Ionics*, 145(14):295 – 306, 2001. Proceedings of the 10th International Conference on Solid State Protonic Conductors.

[48] W. Mnch, K. D. Kreuer, Adams, G. Seifert, and J. Maier. The relation between crystal structure and the formation and mobility of protonic charge carriers in perovskite-type oxides: A case study of y-doped baceo3 and srceo3. *Phase Transitions*, 68(3):567–586, 1999.

[49] K. D. Kreuer, Munch W., Ise M., He T., Fuchs A., Traub U., and Maier J. Defect interactions in proton conducting perovskite-type oxides. *Ber. Bunsenges. Phys. Chem.*, page 214, 1997.

[50] C. Zuo, S. Zha, M. Liu, M. Hatano, and M. Uchiyama. BaZr0.1Ce0.7Y0.2O3-δ as an Electrolyte for Low-Temperature Solid-Oxide Fuel Cells. *Advanced Materials*, 18(24):3318–3320, 2006.

[51] Benjamin H. Rainwater. Electrical properties of $BaZr_{0.1}Ce_{0.7}Y_{0.1}Yb_{0.1}O_{3-\delta}$ and its application in intermediate temperature solid oxide fuel cells, 2012.

[52] T Takahashi and H Iwahara. Solid-state ionics - protonic conduction in perovskite type oxide solid solutions. *Revue de Chimie Minerale*, 17(4):243–253, 1980.

[53] H. Iwahara, T. Esaka, H. Uchida, and N. Maeda. Proton conduction in sintered oxides and its application to steam electrolysis for hydrogen production. *Solid State Ionics*, 34(0):359 – 363, 1981.

[54] M. J. Scholten, J. Schoonman, J. C. Vanmiltenburg, and H. A. J. Oonk. Synthesis of strontium and barium cerate and their reaction with carbon-dioxide. *Solid State Ionics*, 61(1-3):83–91, 1993.

[55] M. J. Scholten, J. Schoonman, J. C. vanMiltenburg, and E. H. P. Cordfunke. The thermodynamic properties of BaCeO3 at temperatures from 5 to 940 K. *Thermochimica Acta*, 268:161–168, 1995.

[56] K. D. Kreuer. Aspects of the formation and mobility of protonic charge carriers and the stability of perovskite-type oxides. *Solid State Ionics*, 125(1-4):285–302, 1999.

[57] Chendong Zuo, S. E. Dorris, U. Balachandran, and Meilin Liu. Effect of Zr-Doping on the Chemical Stability and Hydrogen Permeation of the NiBaCe0.8Y0.2O3- Mixed ProtonicElectronic Conductor. *Chemistry of Materials*, 18(19):4647–4650, 2006.

[58] K. Katahira, Y. Kohchi, T. Shimura, and H. Iwahara. Protonic conduction in zr-substituted baceo3. *Solid State Ionics*, 138(1-2):91–98, 2000.

[59] M. Amsif, D. Marrero-Lopez, J.C. Ruiz-Morales, S.N. Savvin, M. Gabs, and P. Nunez. Influence of rare-earth doping on the microstructure and conductivity of bace0.9ln0.1o3 proton conductors. *Journal of Power Sources*, 196(7):3461 – 3469, 2011.

[60] H. Iwahara, T. Yajima, and H. Ushida. Effect of ionic radii of dopants on mixed ionic conduction in BaCeO3-based electrolytes. *Solid State Ionics*, 7071, Part 1(0):267 – 271, 1994.

[61] Xin-Tai Su, Qing-Zhi Yan, Xiao-Hai Ma, Wen-Feng Zhang, and Chang-Chun Ge. Effect of co-dopant addition on the properties of yttrium and neodymium doped barium cerate electrolyte. *Solid State Ionics*, 177(1112):1041 – 1045, 2006.

[62] Lei Yang, YongMan Choi, Wentao Qin, Haiyan Chen, Kevin Blinn, Mingfei Liu, Ping Liu, Jianming Bai, Trevor A. Tyson, and Meilin Liu. Promotion of water-mediated carbon removal by nanostructured barium oxide/nickel interfaces in solid oxide fuel cells. *Nature Communications*, 2, JUN 2011.

[63] Yong Liu, Lei Yang, Mingfei Liu, Zhiyuan Tang, and Meilin Liu. Enhanced sinterability of BaZr0.1Ce0.7Y0.1Yb0.1O3-δ by addition of nickel oxide. *Journal of Power Sources*, 196(23):9980 – 9984, 2011.

[64] N.P. Bansal. *Advances in Solid Oxide Fuel Cells VI: Ceramic Engineering and Science Proceedings*. Wiley, 2010.

[65] A. Mitterdorfer and L.J. Gauckler. Identification of the reaction mechanism of the Pt, O2(g)—yttria-stabilized zirconia system: Part II: Model implementation, parameter estimation, and validation. *Solid State Ionics*, 117(34):203 – 217, 1999.

[66] J. Fleig. On the width of the electrochemically active region in mixed conducting solid oxide fuel cell cathodes. *Journal of Power Sources*, 105(2):228 – 238, 2002. 7th Ulmer Elektrochemische Tage.

[67] Matthew E. Lynch, David S. Mebane, Yingjie Liu, and Meilin Liu. Triple phase boundary and surface transport in mixed conducting patterned electrodes. *Journal of The Electrochemical Society*, 155(6):B635–B643, 2008.

[68] Junichiro Mizusaki, Hiroaki Tagawa, Kikuji Tsuneyoshi, and Akihiro Sawata. Reaction kinetics and microstructure of the solid oxide fuel cells air electrode la0.6ca0.4mno3/ysz. *Journal of The Electrochemical Society*, 138(7):1867–1873, 1991.

[69] J. Fleig and J. Maier. The impedance of imperfect electrode contacts on solid electrolytes. *Solid State Ionics*, 85(14):17 – 24, 1996. Solid Electrolytes Science and Technology.

[70] G. Beck, H. Fischer, E. Mutoro, V. Srot, K. Petrikowski, E. Tchernychova, M. Wuttig, M. Rhle, B. Lueren, and J. Janek. Epitaxial Pt(111) thin film electrodes on YSZ(111) and YSZ(100) Preparation and characterisation. *Solid State Ionics*, 178(56):327 – 337, 2007.

[71] Alexander K. Opitz and Jrgen Fleig. Investigation of o2 reduction on pt/ysz by means of thin film microelectrodes: The geometry dependence of the electrode impedance. *Solid State Ionics*, 181(1516):684 – 693, 2010.

[72] Junichiro Mizusaki, Hiroaki Tagawa, Takatoshi Saito, Kouji Kamitani, Tamaki Yamamura, Katsuhiko Hirano, Shaw Ehara, Toshinori Takagi, Tomoji Hikita, Masamichi Ippommatsu, Shigeto Nakagawa, and Keiichi Hashimoto. Preparation of Nickel Pattern Electrodes on YSZ and Their Electrochemical Properties in H2H2O Atmospheres. *Journal of the Electrochemical Society*, 141(8):2129–2134, 1994.

[73] A. Bieberle and L.J. Gauckler. Reaction mechanism of ni pattern anodes for solid oxide fuel cells. *Solid State Ionics*, 135(14):337 – 345, 2000. Proceedings of the 12th International Conference on Solid State.

[74] Erik Koep, Charles Compson, Meilin Liu, and Zhiping Zhou. A photolithographic process for investigation of electrode reaction sites in solid oxide fuel cells. *Solid State Ionics*, 176(12):1 – 8, 2005.

[75] H.J. Robota, W. Vielhaber, M.C. Lin, J. Segner, and G. Ertl. Dynamics of interaction of H2 and D2 with Ni(110) and Ni(110) surfaces. *Surface Science*, 155(1):101 – 120, 1985.

[76] K.D. Rendulic, A. Winkler, and H.P. Steinrck. The role of surface defects in the adsorption and sesorption of hydrogen on Ni(111). *Surface Science*, 185(3):469 – 478, 1987.

[77] Matthew E. Lynch, David S. Mebane, Yingjie Liu, and Meilin Liu. Triple phase boundary and surface transport in mixed conducting patterned electrodes. *Journal of The Electrochemical Society*, 155(6):B635–B643, 2008.

[78] David S. Mebane and Meilin Liu. Classical, phenomenological analysis of the kinetics of reactions at the gas-exposed surface of mixed ionic electronic conductors. *Journal of Solid State Electrochemistry*, 10:575–580, 2006.

[79] David S. Mebane and Meilin Liu. Classical, phenomenological analysis of the kinetics of reaction at the gas-exposed surface of mixed ionic electronic conductors: Erratum. *Journal of Solid State Electrochemistry*, 11:448, 2007.

[80] Allen J. Bard and Larry R. Faulkner. *Electrochemical Methods: Fundamentals and Applications*. Wiley, Hoboken, NJ, 2nd edition, 2001.

[81] S.M George, A.M DeSantolo, and R.B Hall. Surface diffusion of hydrogen on Ni(100) studied using laser-induced thermal desorption. *Surface Science*, 159(1):L425 – L432, 1985.

[82] E.G. Seebauer and L.D. Schmidt. Surface diffusion of hydrogen on Pt(111): laser-induced thermal desorption studies. *Chemical Physics Letters*, 123(12):129 – 133, 1986.

[83] D.R. Mullins, B. Roop, S.A. Costello, and J.M. White. Isotope effects in surface diffusion: Hydrogen and deuterium on Ni(100). *Surface Science*, 186(12):67 – 74, 1987.

[84] T. Panczyk and W. Rudzinski. Kinetics of dissociative hydrogen adsorption on the (100) nickel single crystal face: a statistical rate theory approach. *Applied Surface Science*, 233(1-4):141–154, 2004.

[85] Alireza Babaei, San Ping Jiang, and Jian Li. Electrocatalytic Promotion of Palladium Nanoparticles on Hydrogen Oxidation on Ni/GDC Anodes of SOFCs via Spillover. *Journal of The Electrochemical Society*, 156(9):B1022–B1029, 2009.

[86] S. P. Jiang and Y. Ramprakash. H2 oxidation on Ni/YTZP cermet electrodes polarisation behaviour. *Solid State Ionics*, 116(12):145–156, 1999.

[87] Wenping Sun, Mingfei Liu, Shi Feng, Wei Liu, Hyeon Cheol Park, and Meilin Liu. Hydrogen oxidation at the $Pt - BaZr0.1Ce0.7Y0.1Yb0.1O3 - \delta$(BZCYYb) interface. *Phys. Chem. Chem. Phys.*, 15:3820–3826, 2013.

[88] Jan Rossmeisl and Wolfgang G. Bessler. Trends in catalytic activity for SOFC anode materials. *Solid State Ionics*, 178(3132):1694 – 1700, 2008.

[89] Matthew E. Lynch, Dong Ding, William M. Harris, Jeffrey J. Lombardo, George J. Nelson, Wilson K.S. Chiu, and Meilin Liu. Flexible multiphysics simulation of porous electrodes: Conformal to 3D reconstructed microstructures. *Nano Energy*, 2(1):105 – 115, 2013.